学位論文

Application of Atmospheric Millimeter Wave Plasma to Rocket Propulsion

（ミリ波放電大気プラズマのロケット推進への応用）

小田　靖久

Contents

List of Figures

List of Tables

Nomenclature

η :Energy efficiency

$\eta_{\text{absorption}}$:Energy absorption efficiency

η_{coupling} :Energy coupling efficiency

γ :Specific heat capacity ratio

ω :Radius of beam

ρ_n :Density at the region

τ :Pulse duration

τ_{damp} :Time constant of damping period

τ_{osc} :Time constant of oscillation period

A :Area of the thrust wall

a :Acceleration

a_n :Sonic speed at the region

C_{m} :Momentum coupling coefficient

c_{p} :Isobaric specific heat capacity

c_{v} :Isometric specific heat capacity

d :Diameter of the thruster model

F :Thrust force

f :Pulse repetition frequency

I :Impulsive thrust

I_{osc} :Thrust impulse generated by pressure oscillation

I_{plateau} :Thrust impulse generated by plateau pressure

I_{single} :Impulsive thrust at single pulse condition

L :Length of the thruster

l :Normalized plasma length

l_{opt} :Optimum normalized plasma length

L_{plasma} :Plasma traveling length

m :Mass of the thruster model

M_{3C} :Mach number relative to thrust wall

M_n :Mach number at the region

P :Microwave power

$P(\infty)$:Total power of the beam profile

$P(r_{\text{plasma}})$:Partial power radiated on plasma

P_{beam} :Total power on the beam

p_n :Pressure at the region

q :Input Energy

r_{plasma} :Radius of plasma

S :Microwave power density

S^* :Microwave power density when propagation velocity is sonic speed.

S_{ave} :Aaverage power density of the microwave beam profile

S_{peak} :Peak power density of the microwave beam profile

t :Time

t_{plateau} :Duration time of constant pressure at the thrust wall

T_n :Temperature at the region

u :Forced flow velocity in the tube

$U_{\text{expansion}}$:Propagation velocity of expansion wave

U_{ioniz} :Propagation velocity of ionization front

U_{shock} :Propagation velocity of shock wave

u_n :Flow velocity at the region

Chapter 1

Introduction

Recently a low cost space transportation system is strongly demanded for future space development plan, such as future space stations, solar power satellites, and outer planetary exploration.

Chemical rocket engines are conventionary used for the space transportation system. This is because the chemical rocket engine is the only method which can generate large thrust under vacuum environment in space. This situation has not changed since the beginning of the space age when Sputonik was launched as the first artificial satellite.

However the specific impulse of chemical rocket engines are limited only several hundreds second because its thrust power is generated from chemical reaction of on board fuel and oxidizer. Therefore the conventional chemical rocket engine requires huge amount of fuel or propellant for launch from the ground to orbit. Then its payload ratio, the mass ratio of the satellite (payload) to the initial launch vehicle, is limited to only a few percentage. As a result, the launch cost is extremely expensive.

The beamed energy propulsion (BEP) is one of the future low-cost launch systems. Because its propulsive power is provided from the outside of the vehicle, its payload ratio is expected to far higher than the chemical rocket.

In BEP developments, a high power beam generator is the important technology. A GW-class beam would be necessary even for the launcher to Low Earth Orbits. For decades, a GW-class high power beam generator such as the laser oscillator was not developed. Recent high power millimeter wave generators are expected as promising beam source for BEP launchers.

In this thesis, the application of millimeter waves to the BEP was studied. I proposed BEP using s repetitive pulse millimeter wave named Microwave Rocket.

For the first, the millimeter wave technology and studies of BEP are introduced in this chapter.

1.1 Millimeter Wave Technology

Millimeter wave is one of the frequency ranges of the electromagnetic wave. It is also know as a part of microwave and called EHF. The frequency range of millimeter wave is from 30GHz to 300GHz. As is its

name, its wavelength is in millimeter order. Figure 1.1 shows the electromagnetic spectrum.

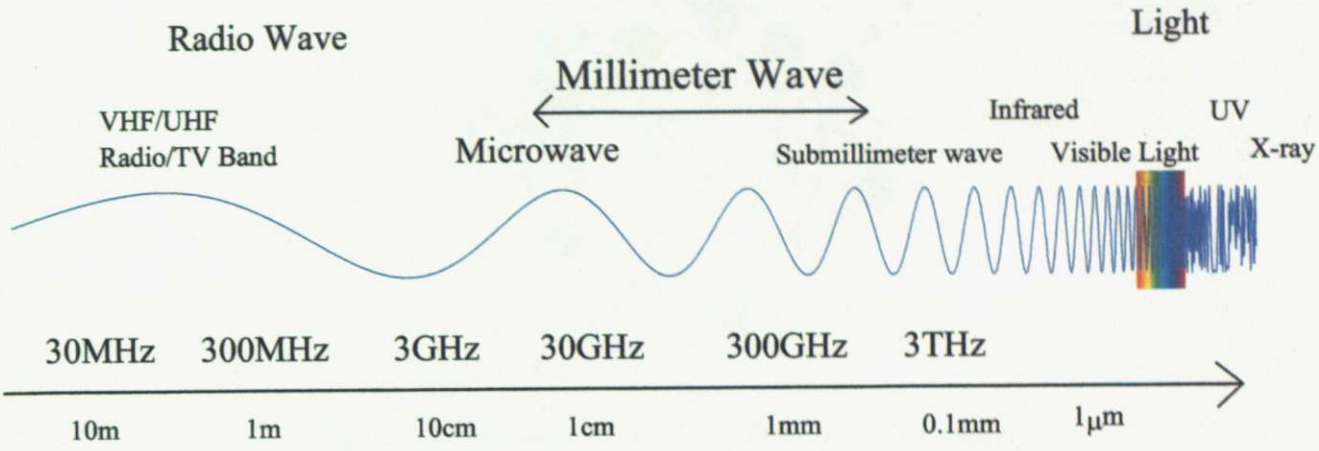

Figure 1.1: Schematic figure of electromagnetic spectrum.

Because millimeter wave is located between the light and radio wave, its behavior is similar to both radio wave and light. Millimeter wave is able to be oscillated or amplified by vacuum tube as same to radio frequency. But millimeter wave is also controlled using optical mirrors. A millimeter wave beam is easily converted from waveguide mode like a laser beam.

1.1.1 High Power Millimeter Wave Generator

Recent progress in the increase in power and frequency of microwave sources has been caused by the development a new branch of physics which can be called high-frequency relativistic electronics. By this term we mean the appearance of microwave sources either based in relativistic effects or using beams of relativistic electrons. Among microwave tubes based on electron bremsstrahlung radiation in a uniform magnetic field, the most common are CRMs(cyclotron resonance maser) or gyrodevices.

The process of phase bunching and energy transfer in CRMs can be well appreciated by referring to Fig.1.2. In Fig.1.2, we see electrons in a magnetic field, executing circular orbits with radii equal to the Larmor radius. The frequency of the rotation is the electron cyclotron frequency. As shown in Fig.1.2, the electrons are homogeneously distributed over their initial phases. In the presence of a traveling electric field rotating synchronously with electrons as would be found in a microwave cavity or waveguide, the electrons gain or lose energy depending on the sign of product of the electric field and the electron velocity. Owing to the energy dependence of the frequency of electron oscillation, the kinetic energy of electrons will be increase or decrease depending on whether energy is lost or gained, resulting in phase bunching.

If the microwave frequency is slightly higher than the cyclotron frequency, the resulting phase bunching in the cyclotron orbit occurs in the decelerating phase of the wave. Then the product of the electron velocity and the electric field is positive quantity for most of the electrons, they lose energy, and there is a net transfer of energy from the electron orbital motion to the microwave field.

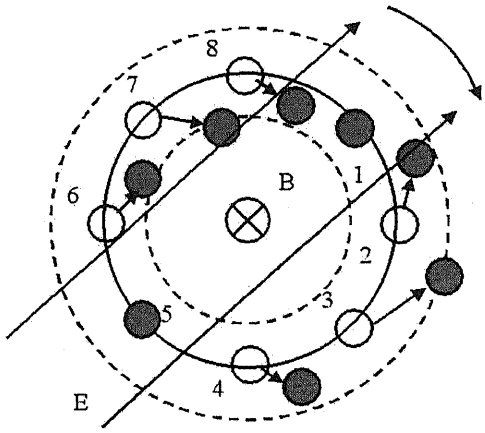

Figure 1.2: Schematic figure of cyclotron resonance maser.

Figure 1.3 shows the configuration of a typical gyrotron. This involved a magnetron injection gun producing an annulus of electrons following helical path along the lines of an axial magnetic field, and a single, open-ended, resonant cavity into which the spiraling electrons were injected.

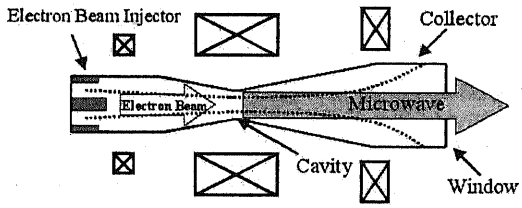

Figure 1.3: Configuration of gyrotron.

In the cavity, the electrons interacted with the microwave field and experienced both phase bunching and transfer of energy to the field. An important advantage of this configuration is the complete separation of the interaction space from the electrodes forming the electron the electron flow. Thus, there is no restriction on operating voltage due to the requirements of avoiding electrostatic breakdown in the interaction space.

Gyro-devices are different from other microwave devices, because the interaction circuit is a high-order-mode cavity allowing higher power at higher-frequency. Their present average power capabilities are plotted versus frequency in Figure , where they can be seen to extend the frequency range of high-power microwave generators by about an order of magnitude compared with the conventional generators based on spatial bunching principles.

The cyclotron resonance maser instability depicted in figure was first described in 1958-59 in the independent work of four scientists, namely, RO.Twiss in Australia, J.Schneider and R.H.Pantell in the United States, and A.V.Gaponov-Grekhov in the USSR.[1]

1.1.2 1MW CW-Gyrotron

At present gyrotrons are mainly used as high power millimeter-wave sources for electron cyclotron resonance heating(ECRH), electron cyclotron current drive(ECCD), stability control and diagnostics of magnetically confined plasmas for generation of energy by controlled thermonuclear fusion. To supply millimeter wave power to International Thermonuclear Experimental Reactor(ITER), 170GHz long pulse gyrotrons are developed all over the world recent decades.[2]

In this study, a high power millimeter wave gyrotron developed at Japan Atomic Energy Agency was used for the beam generator. The designed frequency of the gyrotron was 170GHz. The beam was generated at the cavity exciting $TE_{31,8}$ mode with 6.72 T magnetic field. The beam mode is converted to TEM_{00} gaussian beam by a quasi optical mode conveter in the gyrotron. The gyrotron employs a synthetic diamond output window. The output gaussian beam is transmitted to the experimental site through the corrugated waveguide.

The nominal output of the oscillator was designed as 1MW at steady state continuous-wave output. The maximum pulse length at 1.0MW output was demonstrated up to 1000s in 2006. At 0.6MW output, a demonstraton of 1h was demonstrated. The efficiency of energy conversion from electric energy to electromagnetic wave was achieved 55% with depressed collector. [3] [4]

The scheamtics of the gyrotron configuration and its photograph is shown in Fig.1.4 and 1.5.

The gyrotron of high electric efficiency was developed at Tsukuba university and Japan Atomic Energy Research Institute, their 28GHz-0.5MW gyrotron achieved 50% efficiency without depressed collector.[5]

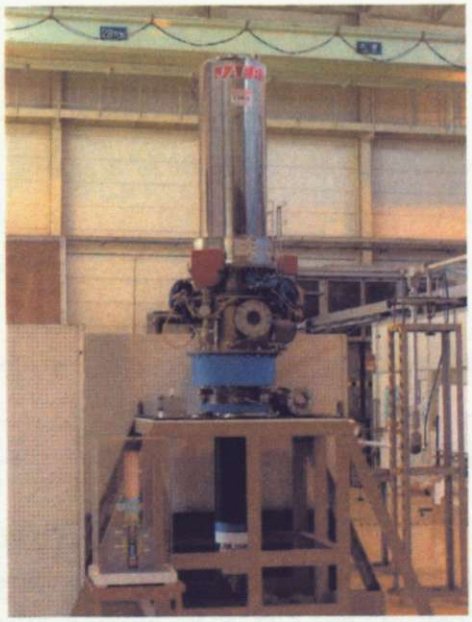

Figure 1.4: 170GHz 1MW-class gyrotron, JAEA

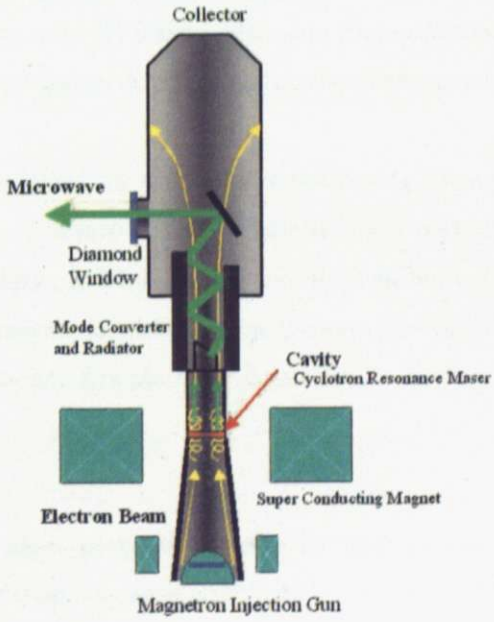

Figure 1.5: Configuration of JAEA long pulse gyrotron

1.1.3 Breakdown in a High Power Millimeter Wave Beam

The breakdown and plasma glow in the high power eloectromagnetic wave field under the atmospheric environment was observed with several wave length and power range. In general, the breakdown occurs under high power density and its threshold field strength has dependence on ambient pressure and wave length. In microwave range, threshold electric field has minimum value 50-100 V/cm around 1 Torr.[6]

The breakdown plasma glows under the high power electromagnetic wave beam absorbing the electromagnetic wave energy. In general, its ionization front propagates towards the electric magnetic wave source. Raizer observed the theoretical model for plasma glow assuming the thermal equilibrium plasma. According to Raizer, theraml conduction at the ionization front and reflection of microwave dominates the propagation. The power density range in his study was 0.2-1.06 kW/cm^2.[7]

In the early 1980s, Brodskii et al. observed an atmospheric discharge under an 85 GHz millimeter-wave beam. The ionization front propagates in the direction of the radiation source at 10-100 m/s. At a power density of $S > 3\,kW/cm^2$, the dependence of propagation velocity of the ionization front U_{ioniz} is quadratic to S.[8] This result shows that U_{ioniz} at the high power-density condition is far greater than predicted by the classical theory based on thermal equilibrium plasma. Instead, they proposed a propagation model with non-equilibrium plasma using ultraviolet radiation.[9] Zorin et al. also pointed out that, in the power density condition of $S > 12\,kW/cm^2$, the ionization front propagates in supersonic velocity.[10][11]

Vikharev et al. observed structure of plasma in the high power millimeter wave beam using 35GHz gyrotron. They took E-plane pictures of the integral structure of dishcharge glow in various gas species. There were three types of the structure depending gas pressure, (1) continuous plasma at low pressure, (2) plasma strips coaxial to the beam at moderate pressure, and (3) plasma filaments perpendicular to the beam (a fish-bone structure) at high pressure. The pressure threshold of changeing the discharge structure had dependence on gas species. [12][13]

Hidaka et al. observed and simulated structure formation of the atmospheric millimeter wave plasma. They observed the array of plasma columns on H-plane structure of the millimeter wave plasma in the 110GHz focused beam using a 1.5MW gyrotron. Each column is forms filaments of the fish-bone structure at E-plane. They pointed out that the array has two-dimensional structure on H-plane and its structure resembled the profile of the millimeter wave diffracting around the plasma column.[14]

1.2 Beamed Energy Propulsion

Beamed energy propulsion (BEP) is the system which gains propulsive energy by high power beamed electromagnetic wave transmitted from outside of the thruster. Because BEP vehicles do not need to load an energy source, such as fuel tank and pump system, heavy electric source, or atomic reactor, the BEP propulsion thruster is very simple. And more, atmospheric air can be utilized as propellant through the flight in the atmosphere, the vehicle can achieve remarkably high payload ratio.

In BEP, once the energy beam station is built, it can be used during many launch counts. The development cost for a beam oscillator is predominant when the launch count is few. The development cost for microwave oscillators is expected two orders of magnitude lower than that of laser, because a GW-class oscillator would be achievable by clustering existing high-power oscillators using the phased array technology. Then, microwave beaming propulsion is expected to achieve lower launch cost with fewer launch counts than laser beaming propulsion.

In open technical literatures, Kantrowitz first proposed in 1972 the concept of launching object using a laser power supplied from a ground-based device.[15] Since that time, beamed energy propulsion has intensively been nominated as a promising method of transporting vehicles with a vastly-low cost.

1.2.1 Laser Propulsion

Currently a majority of researches of BEP is devoted to BEP using a laser beam. The utilizations both of continuous wave(CW) laser and of repetitive pulse (RP) laser have been investigated. As high power laser oscillator was developed in recent years, experimental studies were held in U.S.A., Europe, Russia, China and Japan.

Repetitive Pulsed Air Breathing Thruster

The most famous experiment in laser propulsion was conducted by L.Myrabo et al. in U.S.A.. They launched vertically a small duralmin thruster model with parabolic nozzle called "lightcraft". The momentum coupling coefficient C_m of Lightcraft, the ratio of impulse to input pulse energy, was 126mNs/kJ. In 2000, they had achieved 71m height flight using 10kW-average repetitive pulse laser beam. [16][17]

Laser propulsion using atmospheric discharge by repetitive pulses was proposed and examined. It obtained high thrust performance under atmospheric condition because laser supported detonation under high power laser beam achieves high efficiency in energy conversion.

Laser Thermal Exchange Thruster

The concept of the thermal exchange rocket was proposed and studied by Kare. Instead of using plasma to convert laser energy to thrust force, propellant is heated up to about 2700K and is exhausted using an aerodynamic nozzle. The design concept has similarity to the thermal atomic rocket and high specific impulse ($\sim$ 500-700s) was expected when hydrogen is applied for propellant.[18]

1.2.2 Microwave Propulsion

Researches of Microwave Propulsion

Researches on BEP using a microwave beam were started a few decades ago.

In 1980s, Knecht conducted an analysis on microwave rocket system. In the thruster, propellant is heated by microwave in the dielectric chamber and it is exhausted by nozzle as same to chemical rocket.

Its specific impulse was estimated to 2000s using hydrogen propellant.[19][20]

Batanov also conducted analysis on a microwave rocket using $\lambda = 10\,\mathrm{mm}$ microwave. The rocket nozzle was made from dielectric material to provide microwave power in the rocket. Thrust performance was estimated as $50\,\mathrm{W/kg}$.[21]

Parkin et al. proposed the microwave thermal rocket. In their concept a high power microwave heats a propellant in the dielectric heat exchanger tube and the heated propellant is exhausted using a nozzle as same to the conventional rocket. As same to laser thermal exhchange rocket, propellant is heated up to 2800K and exhausted from a nozzle.[22][23] They measured temperature of helium in a mullite tube using $2.45\,\mathrm{GHz}$ microwave.[24]

Beam Transmission of Microwave Beam

Microwave propagates long distance to provide energy to launch vehicle, for application for BEP launch system. As an electromagnetic beam propagates long distance, beam spot diverges a lot. Diverged spot radius of long propagated electromagnetic beam is obtained from a simple equation for 0th Gaussian mode.

Application of microwave to beamed energy propulsion is limited to frequencies at which the atmosphere is transparent.

The advent of submillimeter astronomy has highlighted the existence of locations with particularly low atmospheric water content, opening up new microwave transmission windows between 35-300GHz and sometimes beyond.

Since the atmospheric scale height of water vapor is only 1-2km, sites such as the Caltech Submillimeter Observatory (CSO) on Mauna Kea are at high altitude, where atmospheric water vapor levels permit transmission above 250GHz, shown in Fig.1.6.

1.2.3 Launch Cost Estimation of BEP

Katsurayama et al. analytically examined feasibility of SSTO system powered by Repetitive Pulse laser and microwave. They proposed a vertical launch to minimize the development cost of the laser base. The vehicle is boosted by beaming propulsion to reach the orbit beyond the GEO. At the apogee point, the vehicle is kicked to a GTO by on-board motor and decelerated at the perigee point as well.

This research considered on the construction of a 100-ton space solar power satellite in GEO. If 1GW-output microwave facility becomes available, a vehicle can launch 100kg payload. Along to their consideration, 1,000 launches are necessary, and cost becomes almost one-tenth of chemical rocket's cost.[25][26][27]

From these previous studies on the concepts and feasibility, the application of the millimeter wave beam to BEP is expected as a promissing technology. Indeed there are few works on the thrust performance of thrust generation of millimeter wave application although its thrust generation mechanism based on physical process is important for further studies.

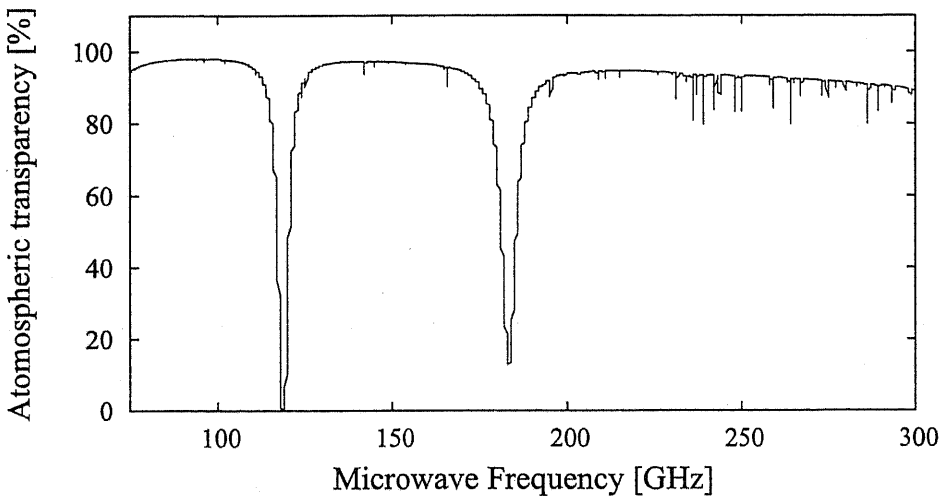

Figure 1.6: Beam transparancy at millimeter wave band.[22]

1.3 Concept of Microwave Rocket

The repetitive pulse microwave beaming propulsion system using microwave breakdown is proposed in this study. Pulsed plasma produced by a high power microwave pulse drives a blast wave. A thruster exhausts the blast wave and acquires impulsive thrust force. This system is called Microwave Rocket. The concept of Microwave Rocket has an advantage on its simple design. A thruster consists of only a focusing reflector substituting an exhaust nozzle. In addition Microwave Rocket can achieve a high payload ratio because Microwave Rocket uses atmospheric air as a propellant during the flight in the atmosphere.

Nakagawa et al. had conducted a single pulse experiment using a conceptual parabolic thruster of Microwave Rocket with a 1MW microwave beam. The measured momentum coupling coefficient C_{m}, defined as a ratio of propulsive impulse to input power, was over 400N/MW.[28]

According to Nakagawa's work, C_{m} decreased with increase of pulse duration. This is due to formation of plasma column. When microwave pulse duration is long, the ionization front of plasma propagates towards microwave source and forms long plasma column. Because the microwave power is absorbed at the ionization front which locates far from the thruster, the most power of long microwave pulse is not converted to thrust force.

To convert most of microwave pulse power to thrust force, a thruster model with a tube is proposed. By this configuration, the most plasma column is contained in the tube. In addition, the microwave beam is provided into the whole part of the thruster like waveguide transmission line.

1.3.1 A Thruster Model

The thruster model is consisted of two parts: a conical nose for plasma ignition and a tube body.

The conical nose focuses the microwave beam on the focusing line. The microwave beam causes the breakdown of atmosphere on the focal line.

In the experimental thruster model, the conical nose part was made of aluminum to reflect and focus the microwave beam. Its apex angle was 60°.

The tube body contains the plasma column. Because the shock wave is formed with the propagation of ionization front of plasma, the tube works as a shock tube. This is similar to a Pulse Detonation Engine. PDE has a tube in which a detonation wave propagates as same to this thruster model.

In the thruster model, two types of tube body with different material were used. One type is made of aluminum and another type is made of acrylic plastic to be able to observe the plasma development inside of the tube. The difference in the shock wave velocity or thrust performance due to material was not found.

1.3.2 Energy Conversion Process

In the tube, the ionization front of plasma absorbs microwave power and isobaric heating at the region produces a heated compression wave and it propagates towards the tube exit. Because the local sonic velocity of heated air is larger than that of initial tube air, it is combined to each other and finally it becomes a normal shock wave. Therefore the shock wave propagates in the tube even detaching from the isobaric heating region. Behind the isobaric heating region, the rarefaction wave follows because of the closed tube end. The plateau pressure region is formed between the end and plasma region. A schematic of distribution of regions is shown in Fig.1.7.

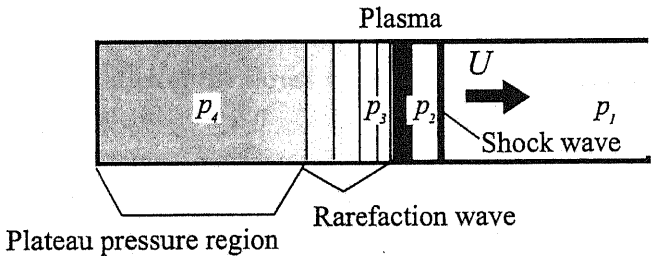

Figure 1.7: Schematics of energy conversion to shcok wave in the tube.

1.3.3 Thrust Generation Cycle

The thrust generation model of Microwave Rocket is explained on the analogy of a pulse detonation engine(PDE). In a PDE, a detonation wave starts from a thrust wall and propagates towards the exit.[29][30]

In Microwave Rocket, a shock wave supported by the microwave plasma propagates in the tube instead of the detonation wave.

Figure 1.8 shows the cycle. The shock wave makes sharp pressure increment and the pressure decreases by the decelerating rarefaction wave. The pressure at the thrust wall is steady until the shock wave is exhausted or terminated. After the termination of the shock wave propagation, an expansion wave goes upstream from the tube exit towards the thrust wall, of which speed is sonic velocity of the constant pressure region. The pressurized air in the thruster is exhausted and pressure decreases to atmospheric pressure. Between the pulses, air in the thruster was scavenged with pressure oscillation.

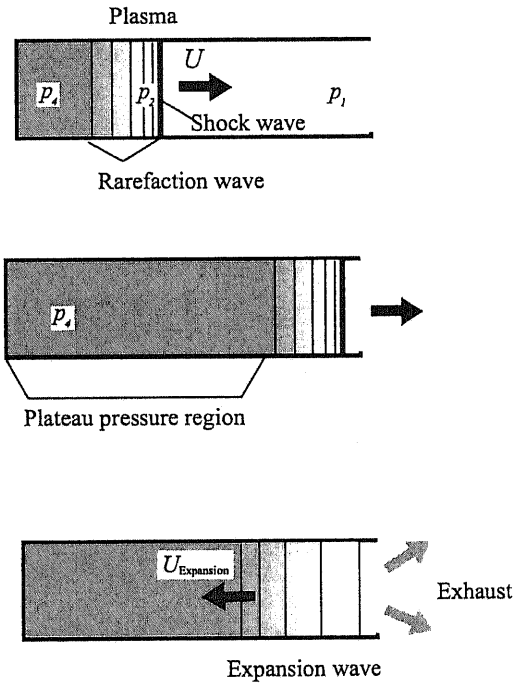

Figure 1.8: Schematics of the thrust generation cycle of Microwave Rocket.

1.4 Objectives

To develop the design method of Microwave Rocket, its thrust generation model was studied.

Firstly physical model of energy conversion at the millimetere wave breakdown was observed at following points.

1. The ignition and development of the atmospheric breakdown using a high power millimeter wave beam was studied.

2. The energy conversion mechanism of the shock wave driven by millimeter wave plasma was studied. The model was verified by measurement of the velocities of the ionization front of plasma and the

shock wave, post-shock pressure, and sonic speed.

Using the energy conversion model, the thrust generation cycle of Microwave Rocket was proposed. The model was verified by measurement results of the thrust performance and thermo-dynamic cycle analysis. The following conditions were observed:

1. Thrust performance dependence on the microwave pulse condition.
2. Continuous thrust generation with microwave pulse repetition and thrust performance dependence on air-refilling condition.
3. Thrust performance dependence on ambient pressure.

Chapter 2

Millimeter Wave Breakdown and its Energy Conversion

2.1 Energy Conversion Model

In the atmospheric breakdown, plasma absorbs power of the millimeter wave beam and the air is heated. Heated air expands quickly and the shock wave is formed. Because the ionization front propagates towards the beam source, the heating region of air also moves following with the ionization front. Therefore shock wave is also propagates with the ionization front converting absorbed millimeter wave energy to fluid energy. The energy conversion model for this phenomenon is studied.

2.1.1 Energy Absorption of Millimeter Wave

On the millimeter wave beam, the electric field and the magnetic field are oscillating at the frequency of the millimeter wave. When plasma is put on the beam, electrons in plasma are accelerated by oscillating electric field and obtain kinetic energy from electromagnetic wave. The accelerated electrons collide with heavy particles, mostly neutral particles, and transfer the absorbed energy to particles in plasma. Therefore fluid is heated by radiation of millimeter wave on the plasma.

Firstly the energy absorption efficiency η was defined for this model, because plasma could absorb a part of millimeter wave beam energy. η is the ratio of absorbed energy to whole beam energy.

η is descried as product of two parameters as followings;

$$\eta = \eta_{\mathrm{coupling}}\eta_{\mathrm{absorption}} \tag{2.1}$$

The beam coupling efficiency η_{coupling} is defined as the ratio of the amount of microwave power irradiated on the ionization front of plasma to total beam power.

When the axis-symmetrical plasma is formed at the center of the Gaussian beam as shown in Fig.2.1,

η_{coupling} is calculated by following equation:

$$\begin{aligned} \eta_{\text{coupling}} &= \frac{P(r_{\text{plasma}})}{P_{\text{beam}}} \\ &= \frac{P(\infty)\left[1-\exp\left(\frac{-2r_{\text{plasma}}^2}{\omega^2}\right)\right]}{P_{\text{beam}}} \end{aligned} \tag{2.2}$$

Here the radius of plasma and radius of the beam are r_{plasma} and ω, respectively.

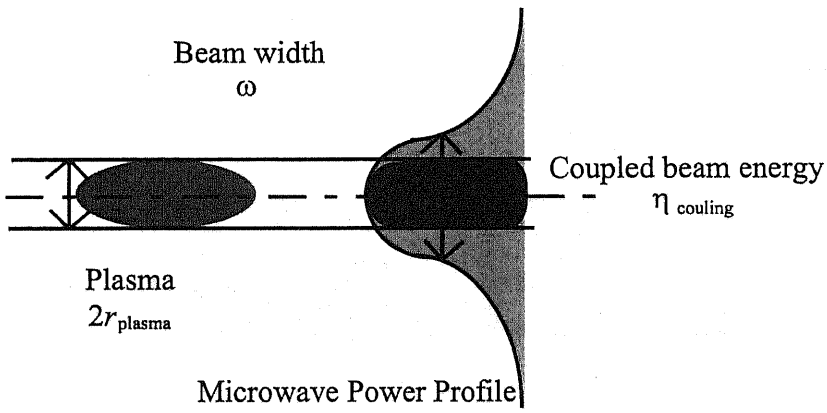

Figure 2.1: Schematics of coupling efficiency definition of microwave beam and plasma.

The absorption efficiency $\eta_{\text{absorption}}$ is defined as the ratio of the net microwave power absorbed by plasma to the amount of microwave power irradiated on the plasma.

In the microwave thermal equilibrium plasma discussed in reference [7], some of microwave beam power is reflected from its surface because plasma has high electron number density.

On the other hand, plasma supported by CW laser cannot exceed the high electron number density which achieves the cut-off frequency for laser's wave length. Therefore some of laser beam power passes through the plasma.

However, in the atmospheric millimeter wave plasma, both reflected and transparent power were not detected during the experiment. Therefore, $\eta_{\text{absorption}} = 1$ in this study.

2.1.2 Microwave Supported Combustion

When an ionization front of plasma propagates in subsonic or transonic, the shock wave and the ionization front are detached from each other. In the case, the defragnation wave resembles the energy conversion process in the closed end tube. In the tube, the ionization front of plasma absorbs microwave power and isobaric heating at the region produces a heated compression wave and it propagates towards the tube exit. Because the local sonic velocity of heated air is larger than that of initial tube air, it is combined to each other and finally it becomes a normal shock wave. Therefore the shock wave propagates in the tube even detaching from the isobaric heating region. Behind the isobaric heating region, the rarefaction wave follows because of the closed tube end. The plateau pressure region is formed between the end and plasma region. A schematic of distribution of regions is shown in Fig.2.2. At the region behind the normal shock, pressure and temperature is represented as p_2 and T_2, respectively. As same, at the plasma region heated by millimeter wave they are p_3 and T_3 and at the constant region behind the rarefaction wave they are p_4 and T_4.

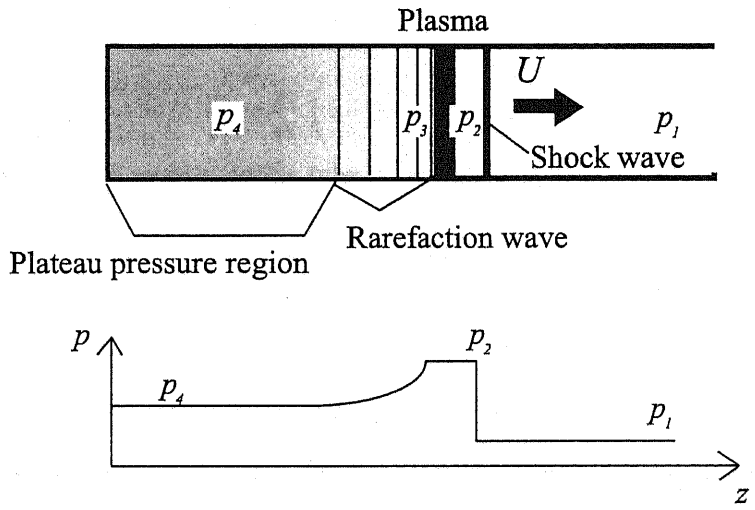

Figure 2.2: Schematics of Microwave Supported Combustion model and pressure distribution in the tube.

Normal shock relations:

$$\frac{p_2}{p_1} = 1 + \frac{2\gamma}{\gamma+1}\left(M_1^2 - 1\right) \tag{2.3}$$

$$\frac{T_2}{T_1} = \left[1 + \frac{2\gamma}{\gamma+1}\left(M_1^2 - 1\right)\right]\left[\frac{2+(\gamma-1)M_1^2}{(\gamma+1)M_1^2}\right] \tag{2.4}$$

$$\frac{\rho_2}{\rho_1} = \frac{u_1}{u_2} = \left(\frac{2+(\gamma-1)M_1^2}{(\gamma+1)M_1^2}\right) \tag{2.5}$$

Here, $M(= u/a)$ is Mach number of flow and γ is the heat capacity ratio. The flow velocity u is the relative velocity to the shock wave surface.

Plasma region relations(isobaric heating):

$$p_2 = p_3 \tag{2.6}$$

$$T_3 = T_2 + \frac{\eta S}{c_p u_2 \rho_2} \tag{2.7}$$

$$\rho_2 u_2 = \rho_3 u_3 \tag{2.8}$$

Here, c_p is isobaric specific heat. The flow velocity u is the relative velocity to the ionization front.

Decelerating rarefaction relations:

$$\frac{p_4}{p_1} = \frac{p_3}{p_1}\left(1 - \frac{\gamma - 1}{2} M_{3C}\right)^{\frac{2\gamma}{\gamma - 1}} \tag{2.9}$$

$$\frac{T_4}{T_1} = \frac{T_3}{T_1}\left(1 - \frac{\gamma - 1}{2} M_{3C}\right)^{2} \tag{2.10}$$

$$\frac{\rho_4}{\rho_1} = \frac{\rho_3}{\rho_1}\left(1 - \frac{\gamma - 1}{2} M_{3C}\right)^{\frac{2}{\gamma - 1}} \tag{2.11}$$

Here, M_{3C} is relative Mach number to the tube. It is expressed with local flow velocities as

$$M_{3C} = \frac{u_3 - u_1}{a_3} \tag{2.12}$$

2.1.3 Microwave Supported Detonation

When the propagation velocity of the shock wave increases, energy conversion process shifts to another process called Microwave Supported Detonation as shown in Fig.2.3.

A detonation wave is a kind of a shock wave driven by heat addition. In the detonation wave, the shock wave induces the chemical reaction or absorption of laser and microwave at shock wave front providing heat into fluid. The shock wave is driven by its local self-heating. The detonation wave propagates in large Mach number because it is necessary to induce the large temperature increment to cause the chemical reaction for heat generation.

The detonation wave more efficiently converts energy to fluid work than the ordinary combustion based on heat transfer process. Therefore the Pulse Detonation Engine(PDE) was expected to achieve higher performance than jet engines based on Brayton cycle. Also in the air breathing laser propulsion, high energy conversion to fluid was observed when the detonation wave was supported by laser power.[]

In the detonation wave, the fluid properties behind the shock wave are determined by following equations;[31]

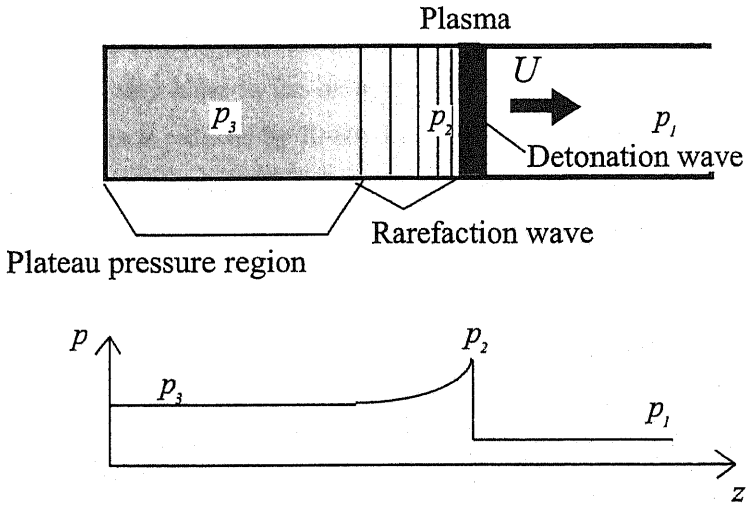

Figure 2.3: Schematics of Microwave Supported Detonation model and pressure distribution in the tube.

$$\begin{aligned} u_1 &= \sqrt{(\gamma_2-1)((\gamma_2+1)\eta q+(\gamma_1+\gamma_1)c_{v1}T_1)/2} \\ &+ \sqrt{(\gamma_2+1)((\gamma_2-1)\eta q+(\gamma_2-\gamma_2)c_{v1}T_1)/2} \end{aligned} \tag{2.13}$$

$$\frac{p_2}{p_1} = \frac{u_1^2+(\gamma_1+1)c_{v1}T_1}{(\gamma_2+1)(\gamma_1-1)c_{v1}T_1} \tag{2.14}$$

$$\frac{\rho_1}{\rho_2} = \frac{u_2}{u_1} = \frac{\gamma_2[u_1^2+(\gamma_1-1)c_{v1}T_1]}{(\gamma_2+1)u_1^2} \tag{2.15}$$

$$c_{v2}T_2 = v_2^2/\gamma_2(\gamma_2-1) \tag{2.16}$$

2.2 Experimental Setup and Measurement Apparatus

2.2.1 Millimeter Wave Beam Generator

A 170 GHz gyrotron, developed as a plasma heating device for the International Thermonuclear Experimental Reactor (ITER), was used as the beam source. Its maximum output power and energy conversion efficiency are, respectively, 1 MW and 50%.

Millimeter waves were guided to the launch site using a corrugated waveguide. A millimeter-wave beam was transmitted from the waveguide outlet through a diamond windows or a Si-N window. Figure 2.4 shows the transmission line and Fig.2.5 shows the waveguide exit with a diamond window. The beam profile was fundamental Gaussian and its beam waist 2ω was 40 mm. The profile is shown in Fig.2.6.

Mid-way of the waveguide, a millimeter-wave detector was set with a directional coupler. The coupler was of the bent type, with several tiny holes in the reflecting mirror to measure millimeter-wave power. The power passing through the holes is reduced by 70-80 dB, and the directivity is 10-20 dB. Using it, histories of millimeter-wave pulses were measured. The detector was calibrated using a calorimetric method with a dummy load settled at the end of the waveguide. The pulse duration was varied from 0.1 ms to 1 ms. Output power was constant during the pulse duration.

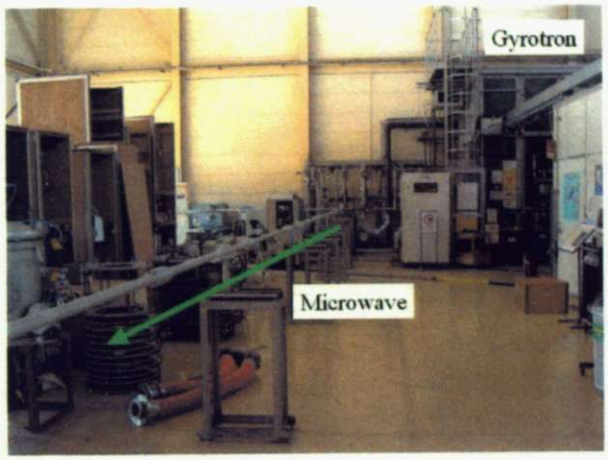

Figure 2.4: Microwave transmiitted to the lauch site using a corrugated waveguide

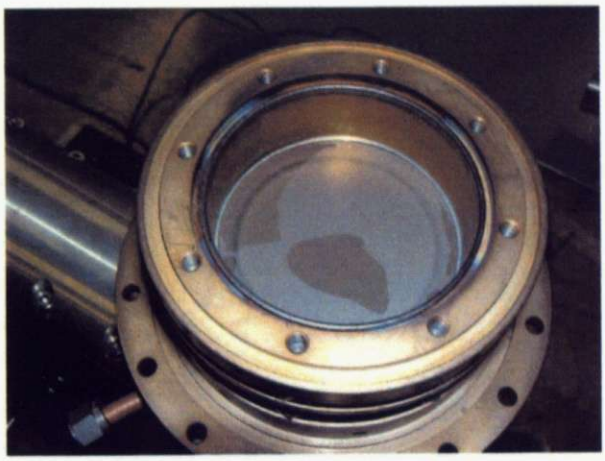

Figure 2.5: Diamond window set to the end of waveguide

2.2.2 Plasma Observation in Free Space

For plasma observation, photographs of the ionization front of the plasma in the reflector were taken using a high-speed framing camera (Fastcam ultima 40 K; Photron Ltd.). To observe plasma ignition process, plasma ignition in the two-dimensional parabolic reflector was observed with the camera position near the reflector shown in Fig.2.8. The focal length and diameter of the reflector were, respectively, 40 mm and 90 mm. The framing speed was 40,500 frame/s.

To observe the development in a millimeter wave beam channel, the camera was set at the other position shown in Fig.2.8. The framing speed was 18,000 frame/s. Plasma was ignited using a three-dimensional parabolic reflector settled 45 cm from the waveguide end. The focal length and diameter of the reflector were, respectively, 15 mm and 90 mm.

2.2.3 Plasma Observation in Tube

A shock wave traveling tube with one closed and one open end was used for measurement of shock wave and ionization front relation. Two tubes were used with different diameter, 40 mm and 60 mm. The length of the tube was 380 mm. A millimeter wave beam is inputted from the open exit and the plasma was

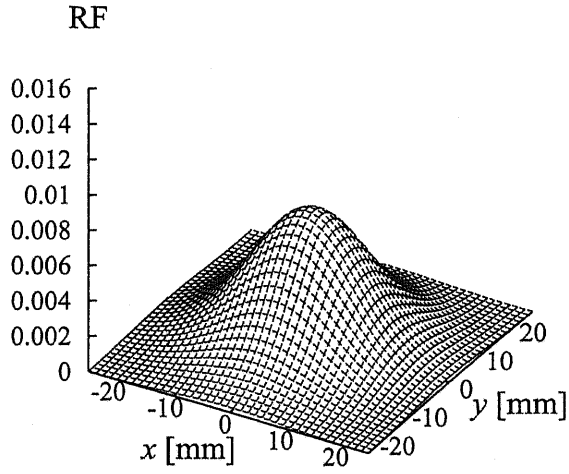

Figure 2.6: Millimeter wave beam profile in free space. $\omega = 20.0\,\mathrm{mm}$

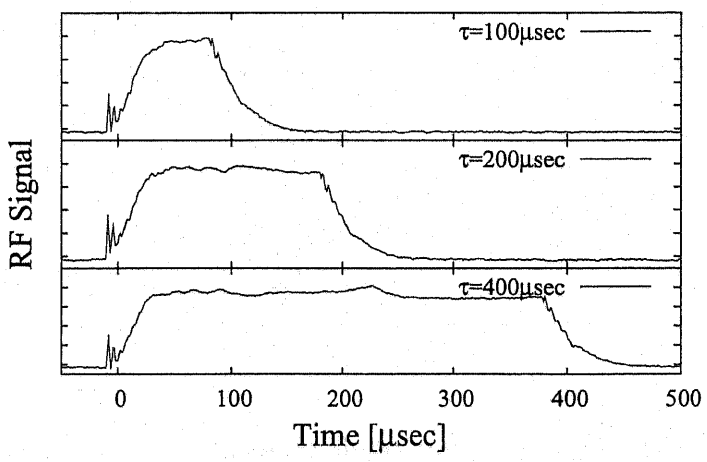

Figure 2.7: Typical signals of microwave pulse

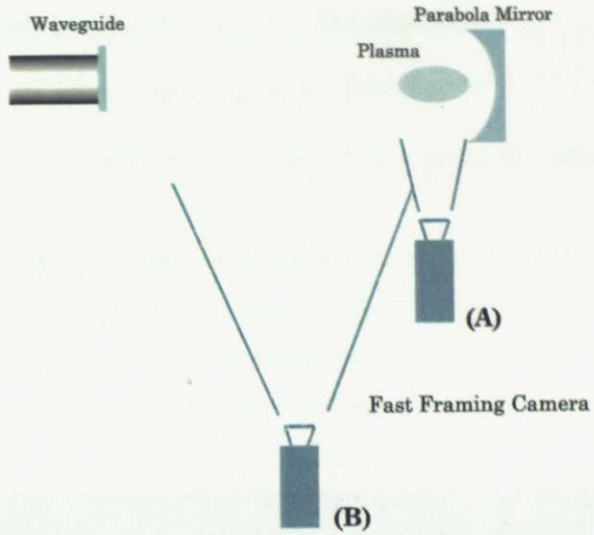

Figure 2.8: Experimental apparatus of plasma observation using a fast raming camera.

ignited at the focal line of the conical nose. The millimeter wave profile in the tube was measured with the low power test.

An ionization front and a shock wave propagate in the tube absorbing microwave power during the microwave pulse. Plasma development in the tube was observed using a high speed framing camera (Fastcam ultima 40K; Photoron Ltd.) to deduce the velocity of an ionization front. The framing speed and exposure time were 18,000 frame/s and 55μs, respectively.

2.2.4 Shock Wave Observation

To measure the velocity of shock wave, two fast pressure gauges (603B; Kistler) were flush-mounted on the tube surface and pressure histories at two positions were recorded at the same time, as shown in Fig.2.9. The distance z from the apex of cone to the gauge was changed from 50 mm to 350 mm.

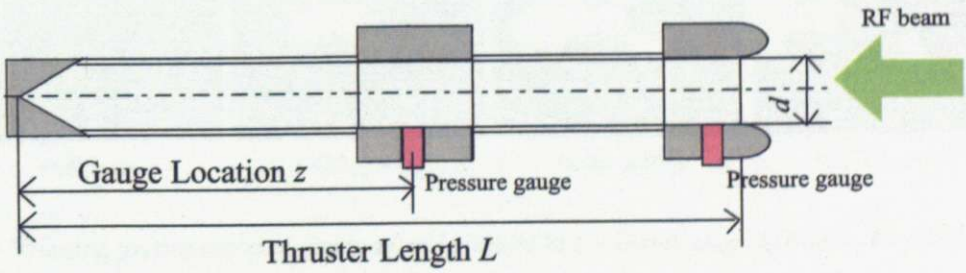

Figure 2.9: Experimental apparatus of pressure history measurement for shock wave observation using pressure gauges.

2.3 Experimental Results and Discussion

2.3.1 Plasma Ignition Process in the Reflector

An atmospheric millimeter wave breakdown was ignited in a parabolic reflector. The formed plasma is shown in Fig.2.10.

Figure 2.11 shows photographs of plasma development inside the 2-D reflector. The discharge was initiated at $t = 0$. The photograph at $t = 0$ shows that the ignition occurs in atmospheric air near the focal point. At the vicinity of focal point, a millimeter-wave beam is focused into the spot, with size nearly equal to its wavelength and power density S is greater than $500\,\mathrm{kW/cm^2}$ when 1 MW power was supplied to the reflector.

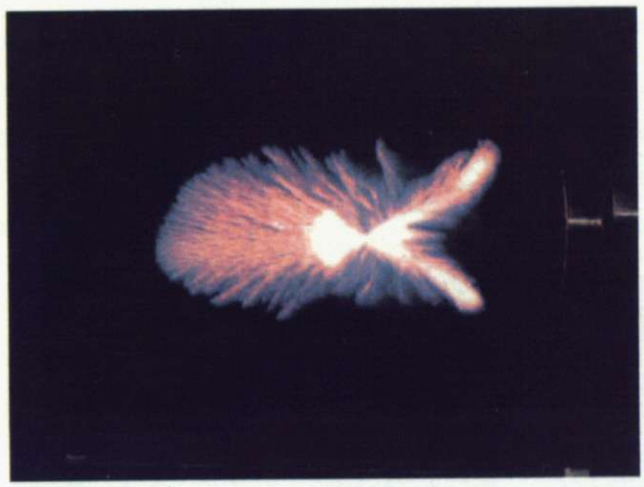

Figure 2.10: Plasma photograph in a 2-D reflector taken home movie camera.

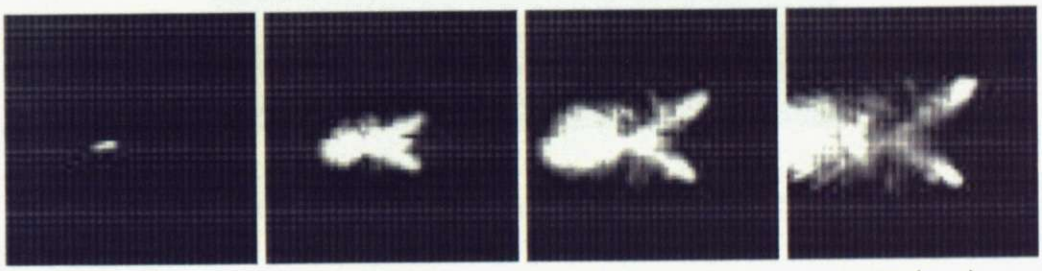

Figure 2.11: Framing photographs of plasma development in a 2-D reflector. 170GHz, P=1MW, 40,500FPS

As the subsequent photographs show, the ionization front propagated in three directions. They are classifiable into two types: a branch on the left-hand side and two spokes on the right-hand side. The left branch absorbs the millimeter-wave beam power provided from the waveguide directly during the pulse duration and grows to a large branch. On the other hand, two small spokes absorb the millimeter-wave reflected on the parabolic reflector. The power density of the reflected millimeter waves is very high at

the time of ignition, but it decreases with time because of the diverging nature of the focused beam and because of the increased fractional absorption by the left branch plasma. The spokes are supported by leakage power and cannot become a large branch.

In addition, although the plasma ignites at the focal point and plasma development in the direction of the reflector finishes in the early period, plasma is detached from the reflector. For that reason, thermal damage to the thruster is expected to be slight, which is advantageous for thruster design.

2.3.2 Propagation Velocity of an Ionization Front in Free Space

The plasma column formed in the millimeter wave beam in free space is shown in Fig.2.12. Figure 2.13 shows side-view photographs of discharge development. As the figure shows, the ionization front propagates upstream of the millimeter-wave beam at a constant velocity. Propagation velocity U_{ioniz} increases with power density S; U_{ioniz} is equal to the sonic velocity $a = 311\,\text{m/s}$ when the power density is $75\,\text{kW/cm}^2 = S^*$. The velocity becomes supersonic at $S > 75\,\text{kW/cm}^2$. The critical power density S^* for supersonic velocity is far greater than $12\,\text{kW/cm}^2$, which was obtained by Zorin et al. at 85 GHz. It might depend on the millimeter-wave frequency.

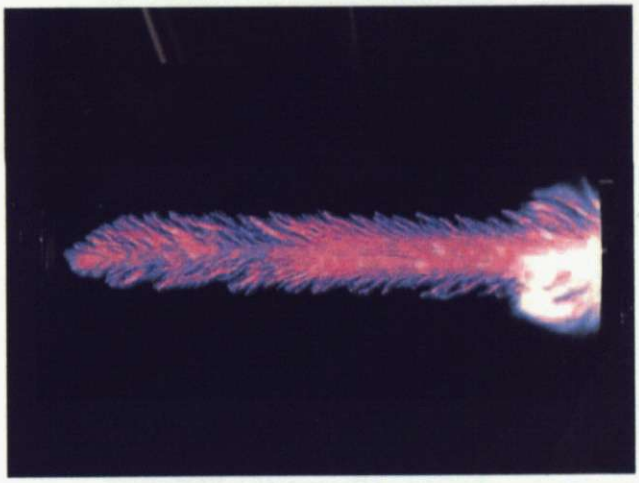

Figure 2.12: Photograph of Microwave Plasma, 700kW, τ=0.4msec

The dependence of the U_{ioniz} and Mach number M on the millimeter wave power density is shown in Fig. 2.14.

2.3.3 Plasma Column in a Tube

An atmospheric millimeter wave breakdown was ignited in a tube and the plasma column is shown in Fig.2.15. Plasma development in a tube was observed using a high speed framing camera. Figure 2.16 shows discharge development in the tube. In the tube, the mode of millimeter wave beam was changed and its peak power density and beam width becomes different from the initial beam profile provided from

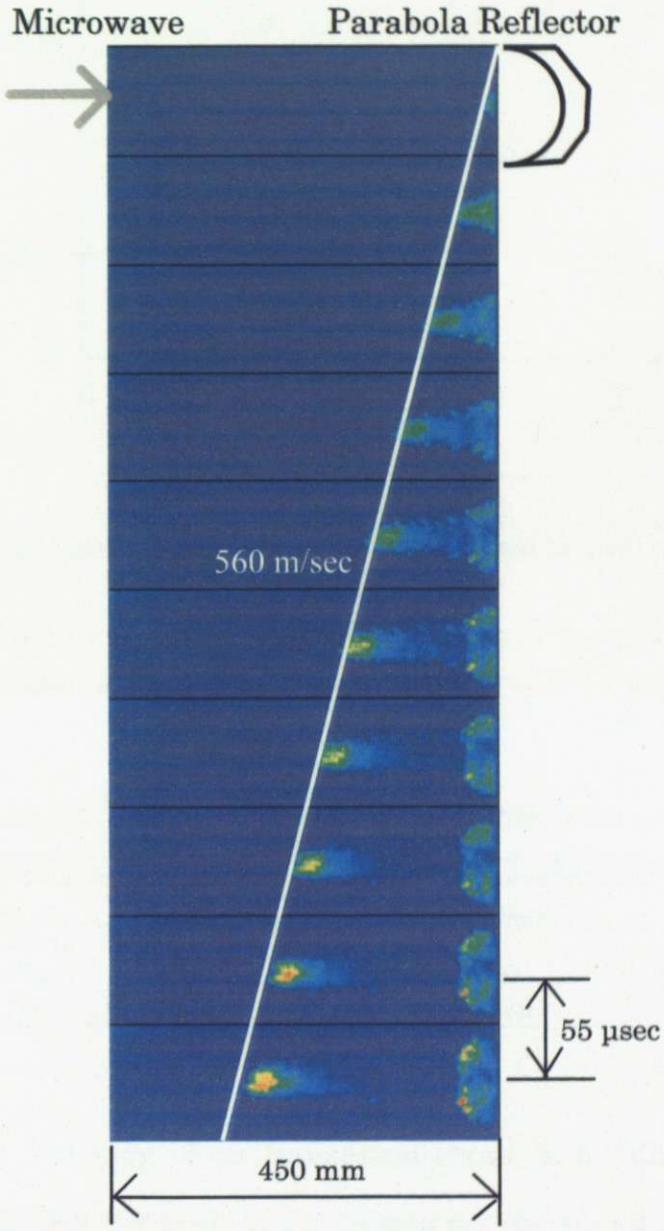

Figure 2.13: Framing photographs of plasma propagation. P=730kW, 170GHz, τ=0.4ms, 18,000FPS

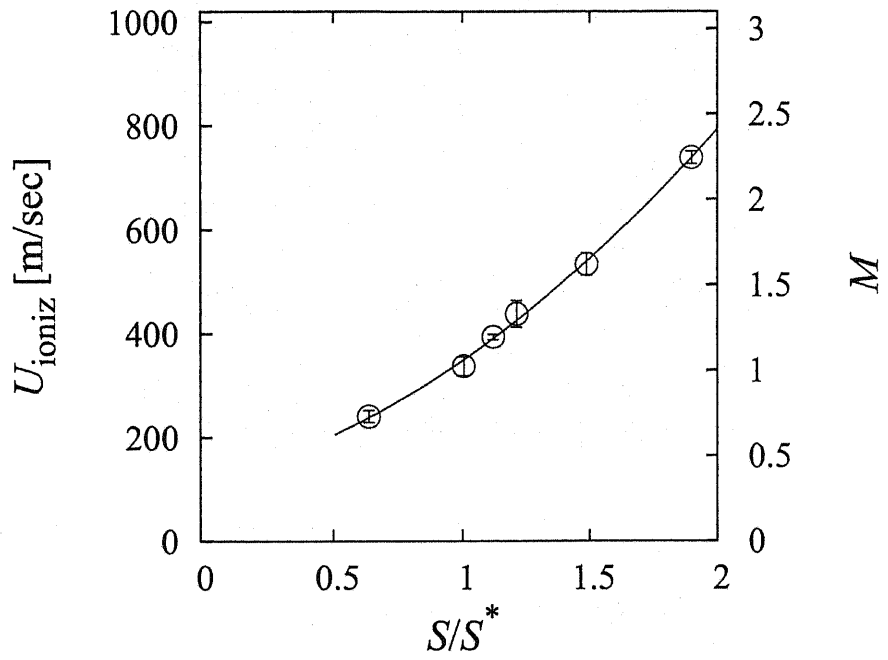

Figure 2.14: Dependence of ionization front velocity U_{ioniz} on millimeter wave power density S, 170GHz

the waveguide exit. Figure 2.17 shows the measured beam profile in the tube. In table 2.1, measured beam profile and the diameter of plasma formed in the tube and beam coupling coefficient η_{coupling} are listed.

Table 2.1: Beam power density and plasma size in the tube

Tube Diameter d	Beam radius ω	Ratio of peak power S/S_{init}	Plasma diameter $2r_{\text{plasma}}$	Beam coupling η_{coupling}
Free Space	21mm	1	-	-
ϕ40mm	10mm	1.73	16mm	0.24
ϕ60mm	18mm	1	25mm	0.48

2.3.4 Propagation Velocity of an Ionization Front in a Tube

Propagation velocity of the ionization front U_{ioniz} in the tube was also deduced. The results of tubes and free space were plotted on Fig.2.18. In Fig.2.18, the horizontal axis is normalized peak power density in each condition. As a result, U_{ioniz} depends on peak power density.

2.3.5 Propagation Velocity of a Shock Wave

The measurement result at the tube surface showed sharp increment of pressure which indicated arrival time of shock wave at each measured point. Each record of pressure gauge revealed constant pressure

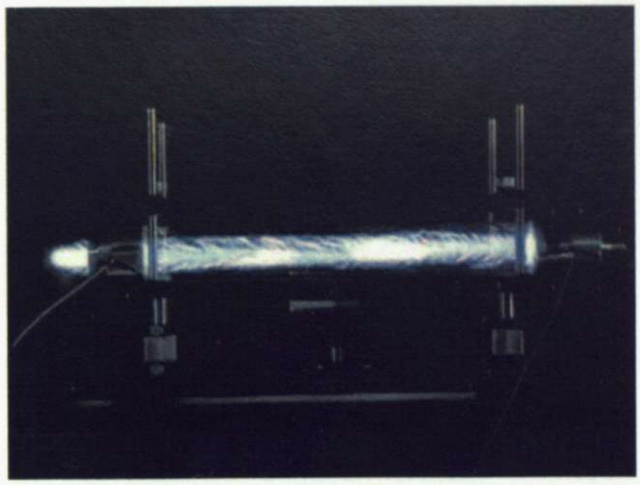

Figure 2.15: Plasma photograph in a ϕ60 mm tube taken home movie camera.

epoch as same to the record at the end and arrival time of expansion wave was found at start time of pressure decrease.

In Fig. 2.19, the arrival time of the shock wave and the expansion wave at each measurement position for $P = 850\,\mathrm{kW}$ condition with ϕ60mm tube was plotted. They showed good linearity and the average propagation velocities of the shock wave and the expansion were deduced.

Figure 2.20 shows the comparison of the velocities of the shock wave and the ionization front propagation. The both velocities were increased with the power density. As shown, when the ionization front propagates on supersonic velocity, both plasma and shock wave propagated in the same velocity.

In Fig.2.20, theoretical CJ-detonation calculation is plotted using Eq.2.13 and estimated η_{coupling}. Although the ionization front and shock wave propagates at the same velocity like a detonation wave, the measured velocity was smaller than theoretical estimation of CJ-detonation.

In Fig.2.21, the relations of detonation wave (Hugoniot relation) are plotted on Pressure-Volume chart. The measurement positions are also plotted. The measured points were located different from CJ point of each Hugoniot relation. In addition, estimated η for measured result using Hugoniot relation was smaller than estimated η from plasma size listed on Table 2.1.

The measured Mach number of the shock wave was small. Because pressure and temperature increment is small, the reaction for microwave absorption would not be induced at the shock front by shock wave itself. Therefore although the shock wave and the ionization front propagated in touch, this propagation mode would be similar to the microwave supported combustion mode instead of the microwave supported detonation mode.

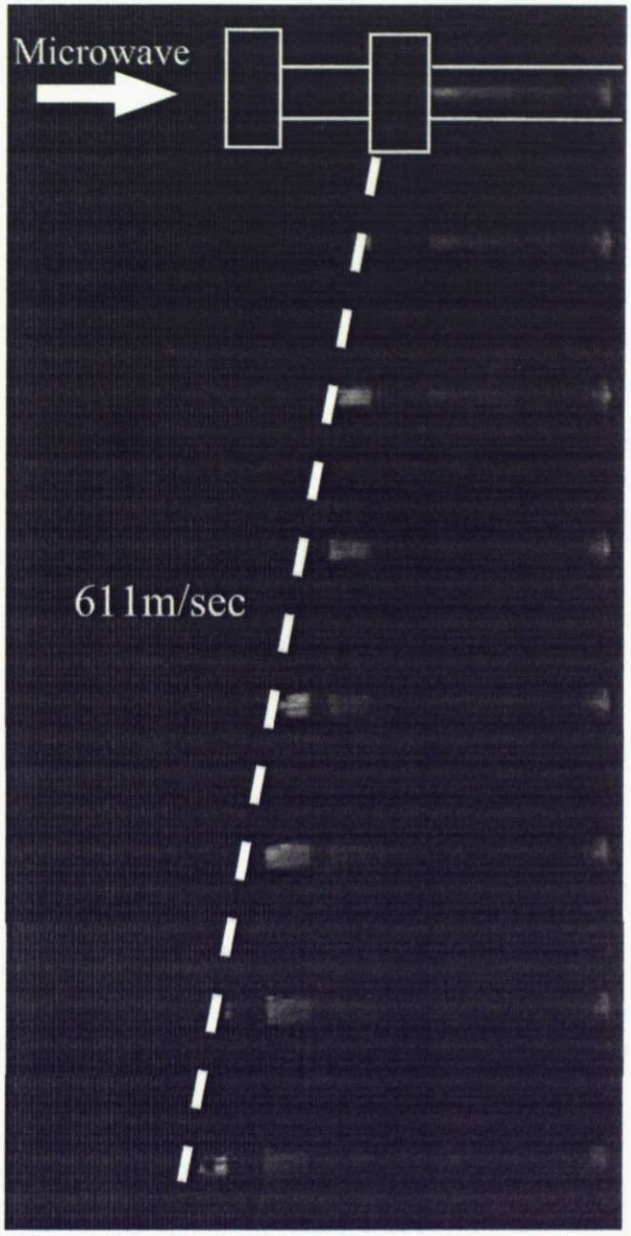

Figure 2.16: Framing photographs of plasma propagationin ϕ40 mm tube. P=850kW, 170GHz, τ=0.4ms, 18,000FPS

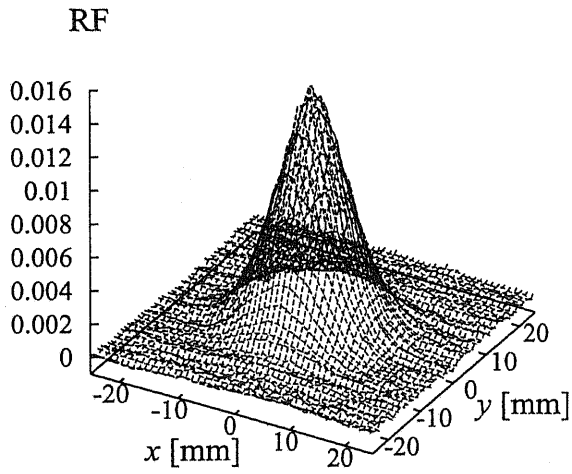

Figure 2.17: Millimeter wave beam profile in ϕ40 mm tube.

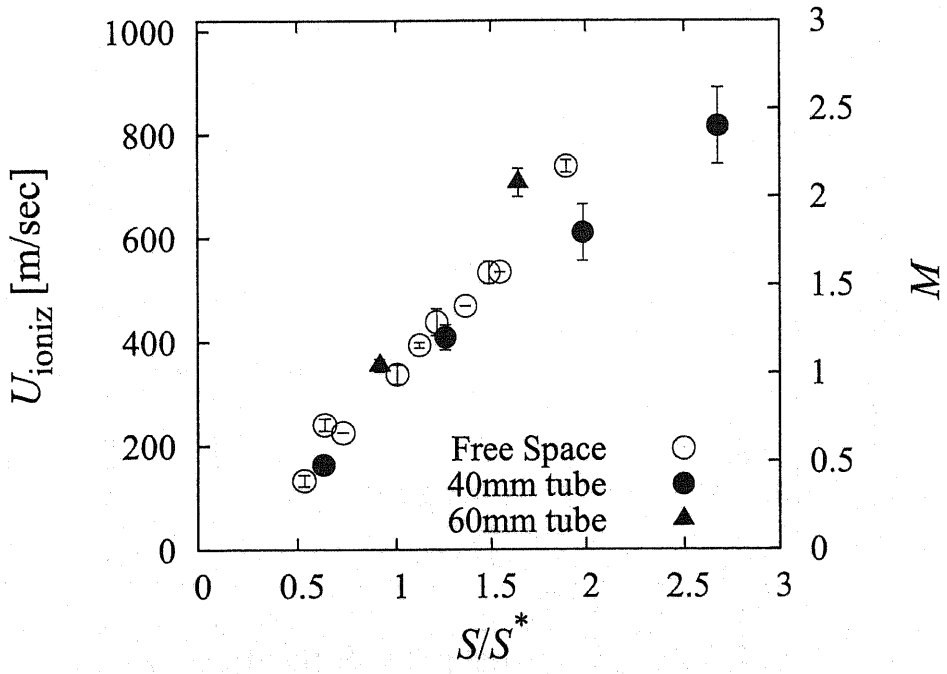

Figure 2.18: Comparison of ionization front velocity U_{ioniz} in free space and in tube; ○: Free space; ●: ϕ40mm tube; ▲: ϕ60mm tube.

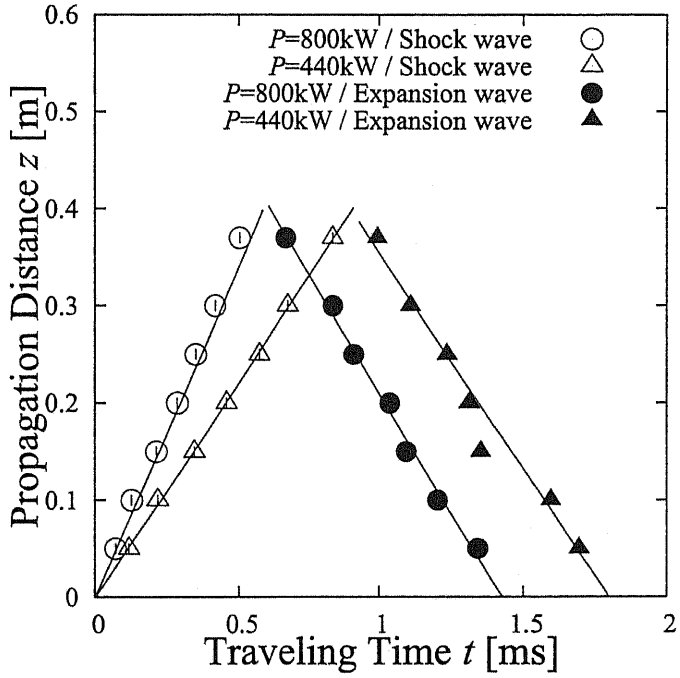

Figure 2.19: Traveling time and propagation distance of shock/expansion waves; ○: P=800 kW shock wave detection; △: P=440 kW shock wave detection; ●: P=800 kW expansion wave detection; ▲: P=440 kW expansion wave detection.

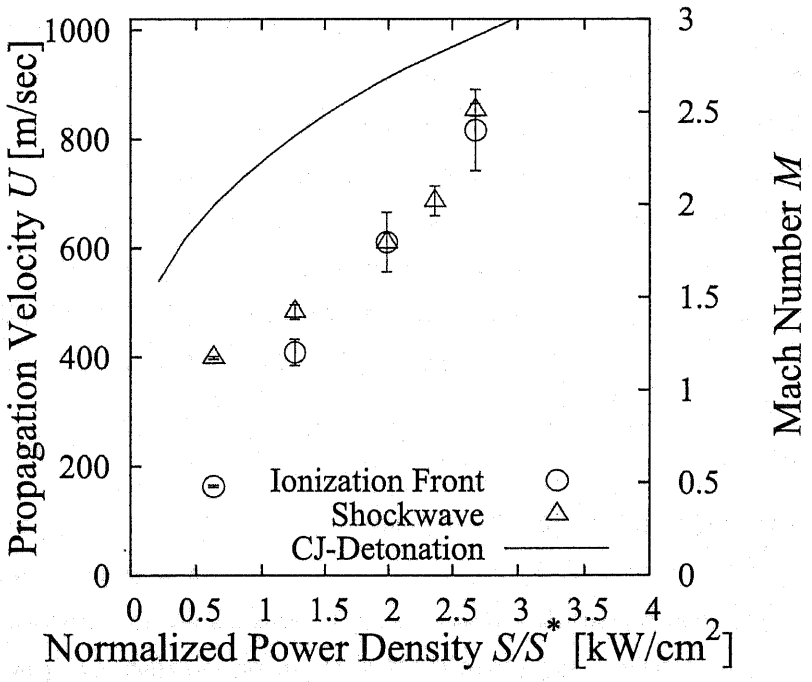

Figure 2.20: Comparison of shock wave and ionization front velocities; ○: The ionization front propagation velocity; △: the shock wave propagation velocity.

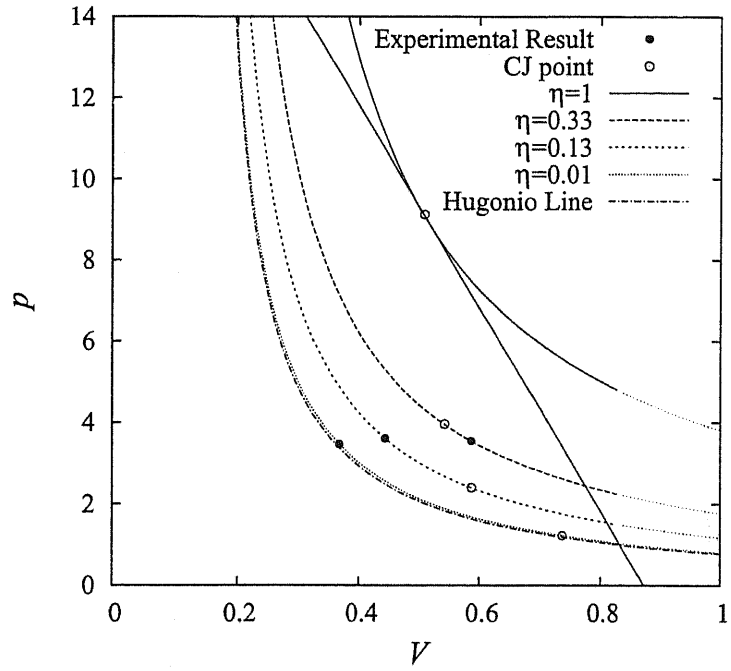

Figure 2.21: Comparison of Hugonio line of theoretical detonation relation and measured result in P-V chart.

2.3.6 Post-shock Properties and MSC Model

Properties behind of the shock wave were measured. The constant pressure behind the rarefaction wave p_4 was measured. Since during the shock wave propagation in the tube the constant pressure at the closed end is kept p_4, measurement results were plotted on Fig.2.22. In Fig.2.22, the dependence of p_4 on power density deduced from the MSC model was plotted. In the model calculation, both propagation velocities of the ionization front and the shock wave were estimated from measurement results in Fig.2.20.

The sonic speed at the constant pressure region was estimated from the velocity of head of pressure decrease. The pressure decrease by exhaust gas propagates at sonic speed. In Fig.2.23, its dependence on the power density is plotted with the MSC model estimation.

2.4 Conclusion

A millimeter wave discharge was ignited in the atmosphere by focusing a millimeter-wave beam with a parabolic reflector at the focal point.

The propagation velocity of the ionization front increased with the millimeter wave power density. It became supersonic at power densities greater than $75\,\mathrm{kW/cm^2}$. The dependence of velocity was identical in free space and in-tube condition.

The ionization front and the shock wave propagated in nearly constant velocity in the tube. When the

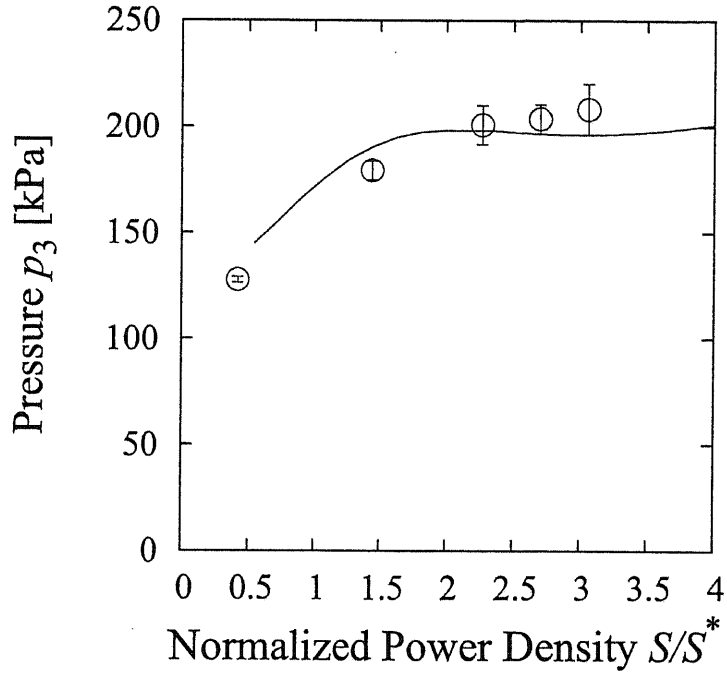

Figure 2.22: Comparison of pressure at the closed tube end, model calculation and measurement result.

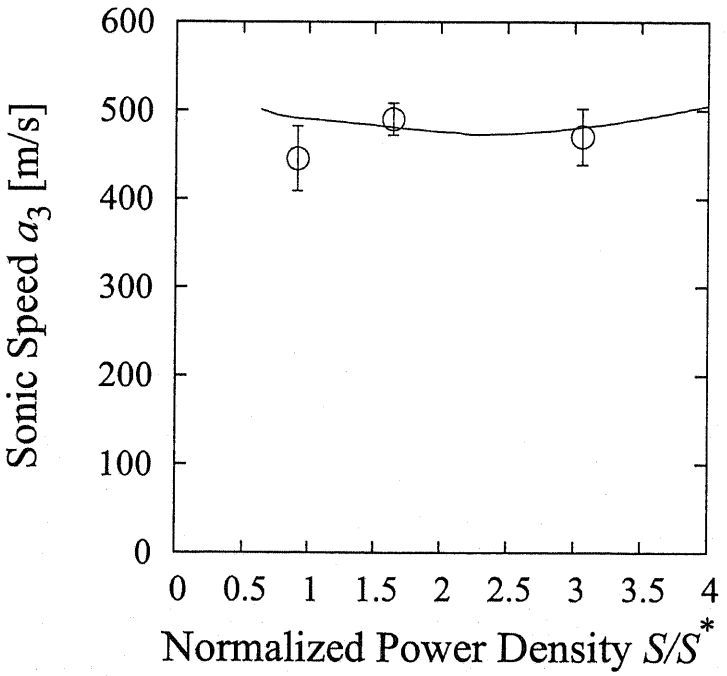

Figure 2.23: Comparison of sonic speed at colsed tube end, model calculation and measurement result(expansion wave velocity)

ionization front propagated at supersonic speed, both velocities were identical.

The MSC model estimation of post-shock wave pressure and sonic speed using estimated η_{coupling} resembled the measurement result.

As a conclusion, the energy conversion mechanism in millimeter wave breakdown is explained by the MSC model.

Chapter 3

Thrust Performance of Microwave Rocket

3.1 Thrust Generation Cycle

The thrust generation model of Microwave Rocket is explained on the analogy of a pulse detonation engine(PDE). In a PDE, a detonation wave starts from a thrust wall and propagates towards the exit. In Microwave Rocket, a shock wave supported by the microwave plasma propagates in the tube instead of the detonation wave.

Figure 3.1 shows the cycle. The shock wave makes sharp pressure increment and the pressure decreases by the decelerating rarefaction wave. The pressure at the thrust wall is constant until the shock wave is exhausted or terminated. After the termination of the shock wave propagation, an expansion wave goes upstream from the tube exit towards the thrust wall, of which speed is sonic velocity of the constant pressure region. The pressurized air in the thruster is exhausted and pressure decreases to atmospheric pressure. Between the pulses, air in the thruster was scavenged with pressure oscillation.

Normal shock relations:

$$\frac{p_2}{p_1} = 1 + \frac{2\gamma}{\gamma+1}\left(M(S_{\text{peak}})^2 - 1\right) \tag{3.1}$$

$$\frac{T_2}{T_1} = \left[1 + \frac{2\gamma}{\gamma+1}\left(M(S_{\text{peak}})^2 - 1\right)\right]\left[\frac{2+(\gamma-1)M_1^2}{(\gamma+1)M_1^2}\right] \tag{3.2}$$

Here, S_{peak} is the peak power density of the microwave beam profile. For Gaussian beam,

$$S_{\text{peak}} = P_{\text{beam}}\frac{2}{\pi\omega^2} \tag{3.3}$$

Plasma region relations(isobaric heating):

$$p_2 = p_3 \tag{3.4}$$

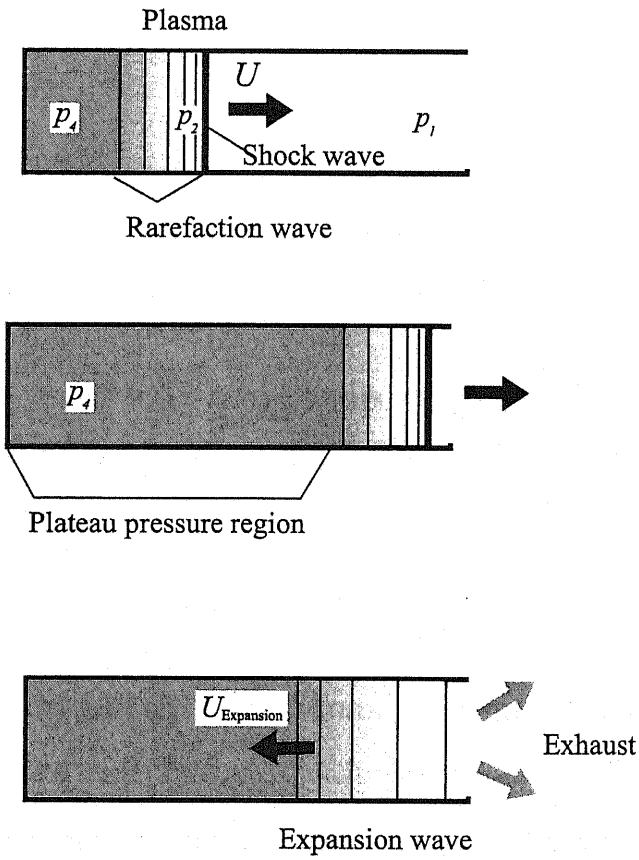

Figure 3.1: Schematics of the thrust generation cycle of Microwave Rocket.

$$T_3 = T_2 + \frac{\eta S_{\text{ave}}}{c_p u_2 \rho_2} \tag{3.5}$$

Here, S_{ave} is the average power density of the microwave beam profile. For ϕd thruster model,

$$S_{\text{ave}} = \frac{P_{\text{beam}}}{\pi d^2/4} \tag{3.6}$$

Decelerating rarefaction relations:

$$\frac{p_4}{p_1} = \frac{p_3}{p_1}\left(1 - \frac{\gamma - 1}{2} M_{3C}\right)^{\frac{2\gamma}{\gamma - 1}} \tag{3.7}$$

$$\frac{T_4}{T_1} = \frac{T_3}{T_1}\left(1 - \frac{\gamma - 1}{2} M_{3C}\right)^{2} \tag{3.8}$$

$$M_{3C} = \frac{u_3 - u_1}{a_3} \tag{3.9}$$

Total impulsive thrust I for a single cycle operation is calculated as,

$$I = \int (p - p_1) A dt = (p_4 - p_1) A t_{\text{plateau}} \tag{3.10}$$

Here, A is the area of the thrust wall, and t_{plateau} is the duration time of constant pressure at the thrust wall. t_{plateau} is calculated as

$$t_{\text{plateau}} = \frac{L}{U_{\text{shock}}} + \frac{L}{U_{\text{expansion}}} \tag{3.11}$$

3.2 Experimental Setup and Measurement Apparatus

3.2.1 Vertical Launch and Thrust Measurement

Figure 3.2 shows the schematics of a cone-tube thruster models. Two different cylinder lengths were tested: their respective total lengths L were designed as 180 mm and 380 mm. The diameter of the tube was 60 mm.

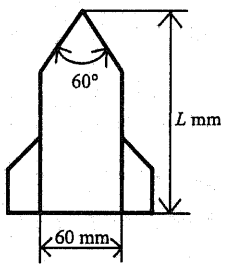

Figure 3.2: Schematics of thruster models.

The conical nose focuses a millimeter wave beam on the axis to initiate the discharge in the thruster. The discharge was ignited without misfiring. The thruster models were launched vertically. Their flight trajectories were recorded using a laser displacement sensor (LB-2; Keyence Co.). Obtained thrust impulses were estimated by curve fitting of the parabolic trajectory of the thruster. The aerodynamic drag was negligibly small because the maximum velocity during the flight was maintained at less than 1 m/s. Its schematics and photograph is shown in Fig.3.3 and Fig.3.4.

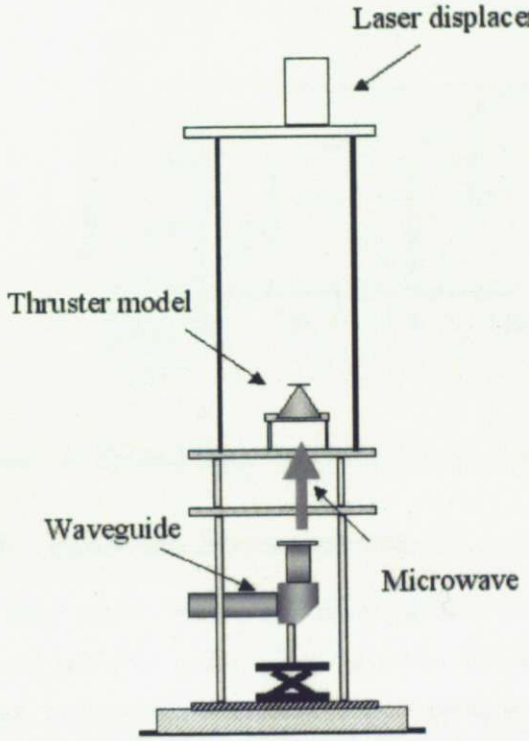

Figure 3.3: Thrust measurement settings by vertical flight experiment

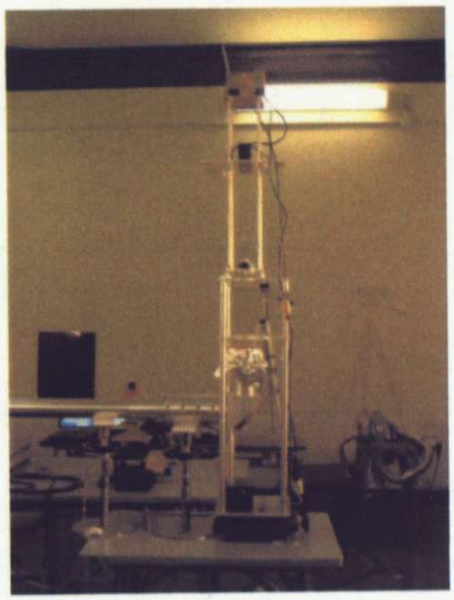

Figure 3.4: Photograph of thruster mesurement setting in microwave sealed room, JAEA

For thrust measurement with repetitive pulses, conical thruster models and a cone-tube thruster model were used. The conical thruster models' generating line length were 40 mm and 90 mm, and both apex angle were 60°. The millimeter wave beam was inputted from the base and focused on the centerline. The length of the cone-tube thruster model used in repetitive pulse operation was L=111 mm. Its diameter was ϕ60 mm.

Thruster models were launched vertically and their flight trajectories were recorded using a laser displacement gauge. Typical flight trajectories at both single and multi pulse operation are plotted in Fig.3.5. The initial velocity was calculated from the trajectory and the impulsive thrust was deduced for pulse by pulse.

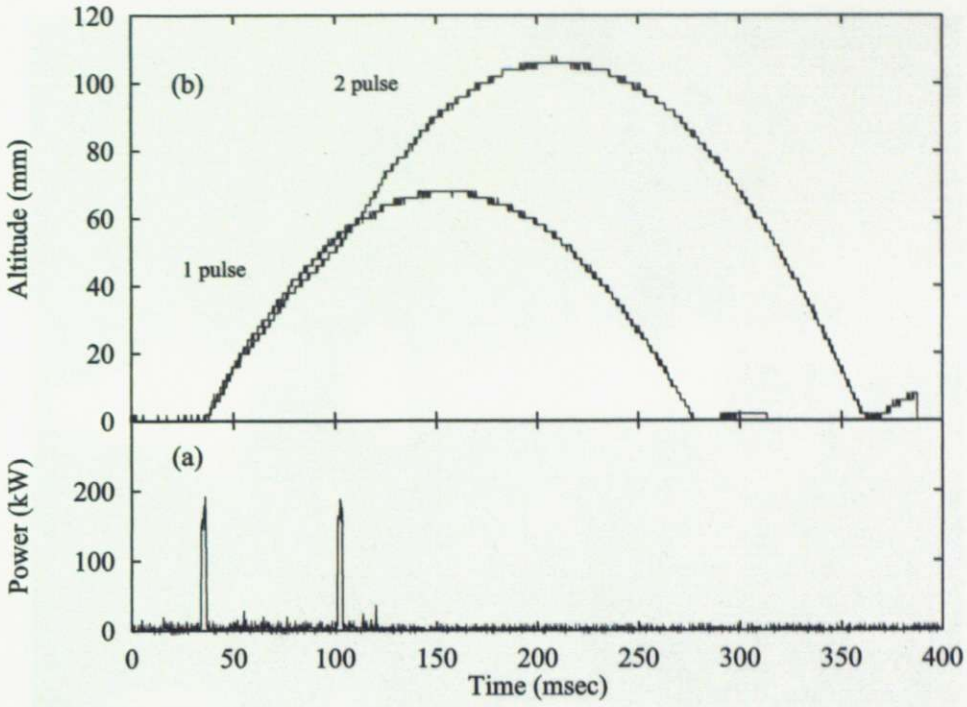

Figure 3.5: Typical flight trajectory and microwave pulse history. $P = 200$ kW, repetition rate 15 Hz

3.2.2 Pressure Measurement

A thruster model composed of a conical nose (thrust wall) and a tube was used for the pressure measurement as shown in Fig.3.6 and Fig.3.7. The total length and diameter of the tube were 380 mm and ϕ60 mm, respectively. A millimeter wave beam is inputted from the tube exit and the plasma was ignited at the focal line of the nose cone.

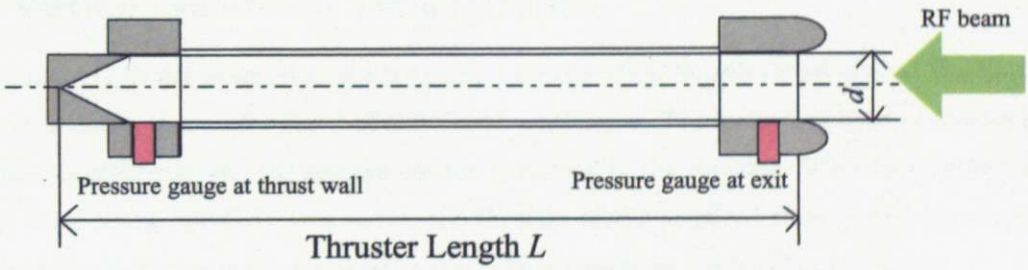

Figure 3.6: Experimental apparatus of pressure history measurement at thrust wall for thrust measurement using a pressure gauge.

To measure the velocity of shock wave, two fast pressure gauges (603B; Kistler) were flush-mounted on the tube surface and pressure histories at two positions were recorded at the same time. One gauge was set near the thrust wall and the other gauge was set near the thruster exit. Using the difference of shock wave arrival time, the average shock wave propagation velocity in the thruster was deduced.

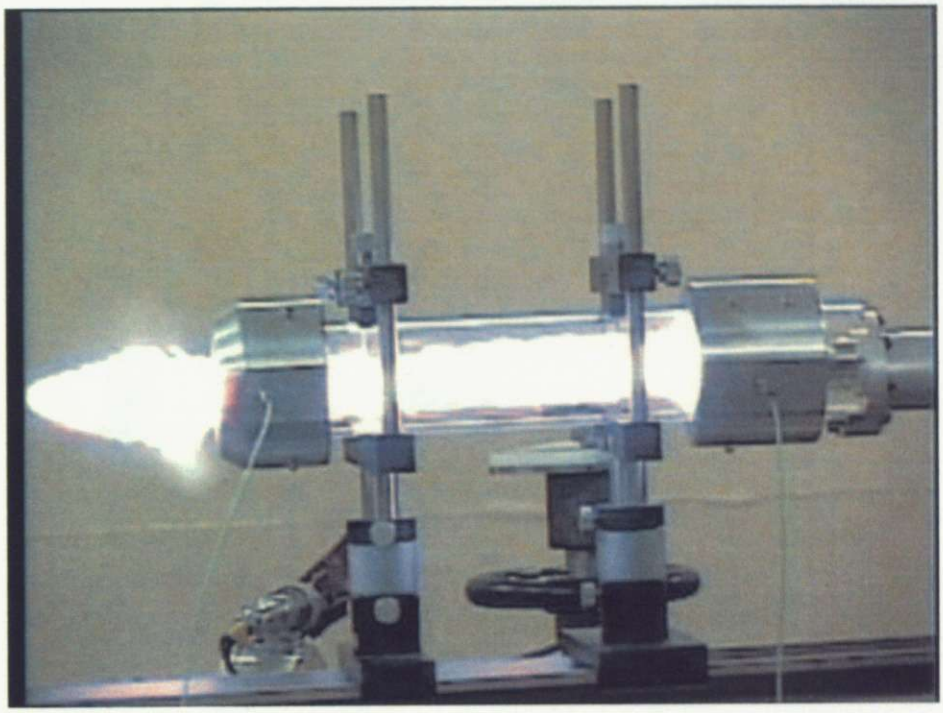

Figure 3.7: Thruster model for pressure measurement is under operation.

The pressure history at the thrust wall and the measurement result of the shock wave propagation velocity was also measured for thrust estimation. For this measurement, the thruster length L was also varied from 198 mm to 573 mm for the ϕ60 mm tube.

3.3 Experimental Results and Discussion

3.3.1 Vertical Launch and Thrust Impulse

The experiment of thrust generation was conducted using vertical launch thrust stand. The thruster model successfully ignited plasma with input of millimeter wave beam. The ionization front of plasma propagates towards the thruster exit and the column plasma is formed in the thruster. With atmospheric breakdown the thrust force was generated. As a result, the thruster model acquired velocity and launched vertically. The recorded trajectory was the parabolic curve which resembles the free fall trajectory.

Measurement of the thrust impulse for each thruster was conducted for the power range of 320-850 kW. The measured thrust impulse was plotted on Fig.3.8. When the pulse duration τ is smaller than certain condition, the impulse increases with increase of pulse duration. Indeed the increment of impulse is saturated and the maximum impulse for each thruster is obtained when τ exceeds the condition.

The maximum τ condition has dependence on the thruster length L. The maximum τ is obtained when the traveling length of the ionization front $U_{\mathrm{ioniz}}\tau$ is identical to L.

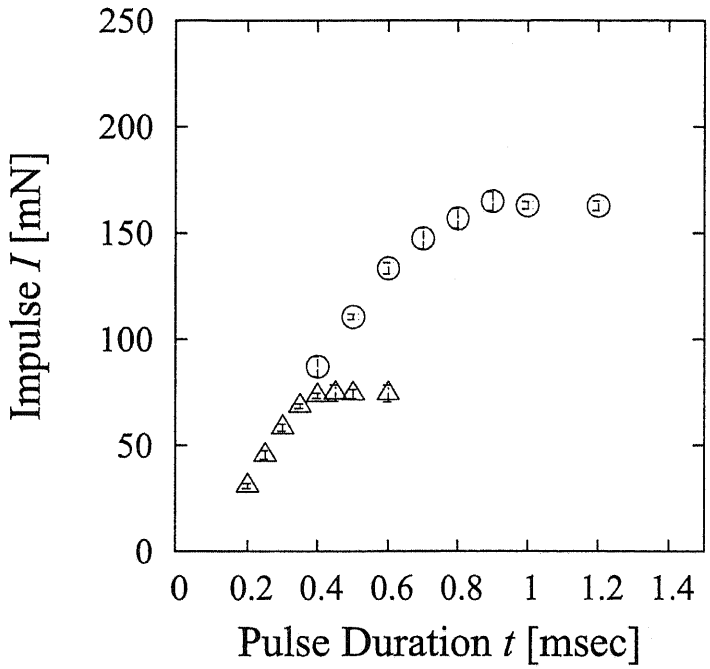

Figure 3.8: Dependence of Impulse I on the microwave pulse duration τ; ○: $L = 380\,\mathrm{mm}$ thruster model at $S_{\mathrm{peak}} = 98\,\mathrm{kW/cm^2}$, △: $L = 180\,\mathrm{mm}$ thruster model at $S_{\mathrm{peak}} = 98\,\mathrm{kW/cm^2}$

3.3.2 Thrust Impulse with Pulse Repetition

Thrust measurement under the multi pulse operation was conducted. Two pulses with various interval durations were inputted into the thrusters at each operation.

Figure 3.9 shows the dependence of the thrust impulse imparted by the second pulse on the repetition frequency. When the repetition frequency is smaller than the critical frequency, the impulse saturates. Their critical frequency depends on with the thruster scale. For the 40 mm conical thruster, its critical frequency was 50 Hz. However, for the 90 mm conical thruster and the cone-tube thruster, their critical duration was larger than 30 Hz.

3.3.3 Pressure History at Thrust Wall and Thrust Estimation

Figure 3.10 shows the measured pressure history at the thrust wall under the condition of microwave pulse duration of 0.4 ms and 800 kW, in which the traveling distance of the ionization front was nearly identical to the thruster length. Firstly, sharp and large pressure increment appeared and decreased quickly. Then pressure was constant during the propagation of the shock and expansion waves, and started to decrease when the expansion wave arrived at the thrust wall.

Thrust impulse I was estimated using Eq.3.12. The estimated thrust from pressure history was far larger than the result of the flight experiment.

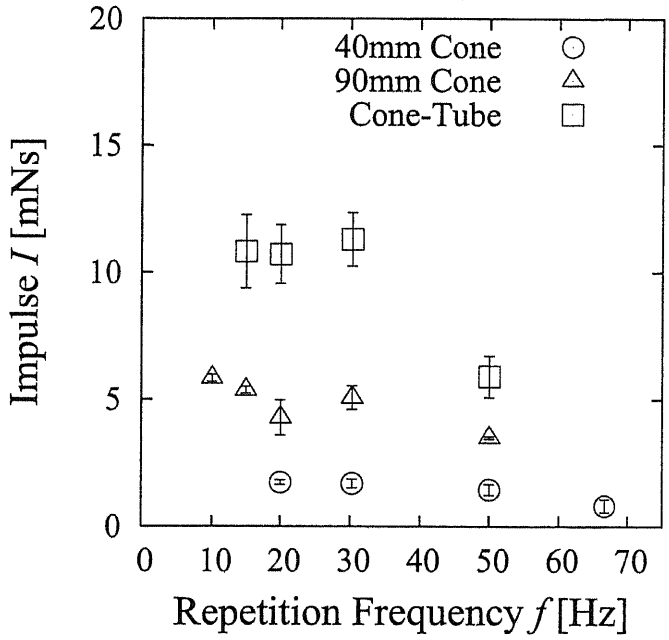

Figure 3.9: Result of thrust measurement on double pulsed vertical flight experiment. Dependence of impulse on repetition frequency.

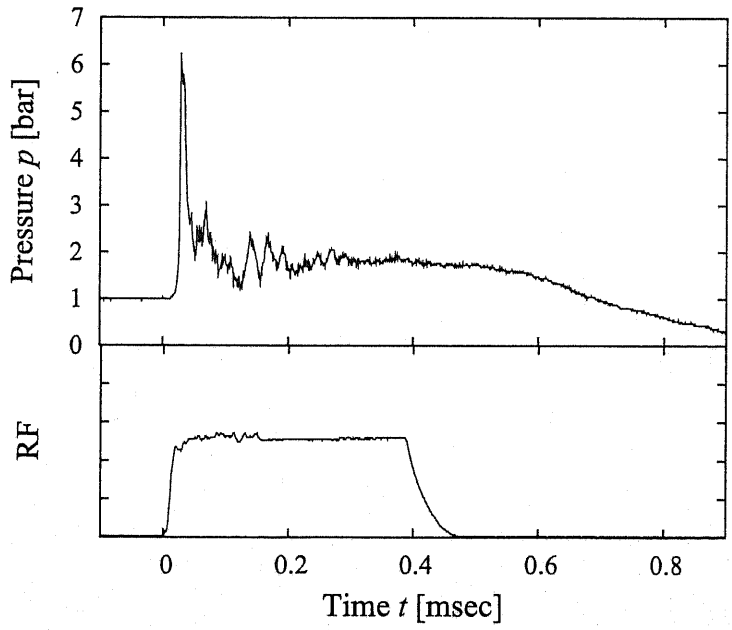

Figure 3.10: Pressure history at the thrust wall and microwave pulse history.

This difference between the flight experiment and the pressure measurement is due to two reasons: 1) the interference of exhaust gas at thruster exit at launch experiment: 2) the launch stand and the negative thrust by pressure oscillation of air-refilling process at pressure measurement.

At flight experiment, the thruster model is put on the launch stand. The ϕ60mm thruster is setup on the ϕ75mm beam input hole fabricated on the thruster setup stage. To measure the thrust performance of thruster put in the free space, the thruster model was hanged from the up stage of the thrust stand. Figure 3.11 shows the measurement result of I of the thruster hanged 150mm from the launch stage with comparison of the thruster on the launch stage. The larger I was obtained in free space than the launch stage.

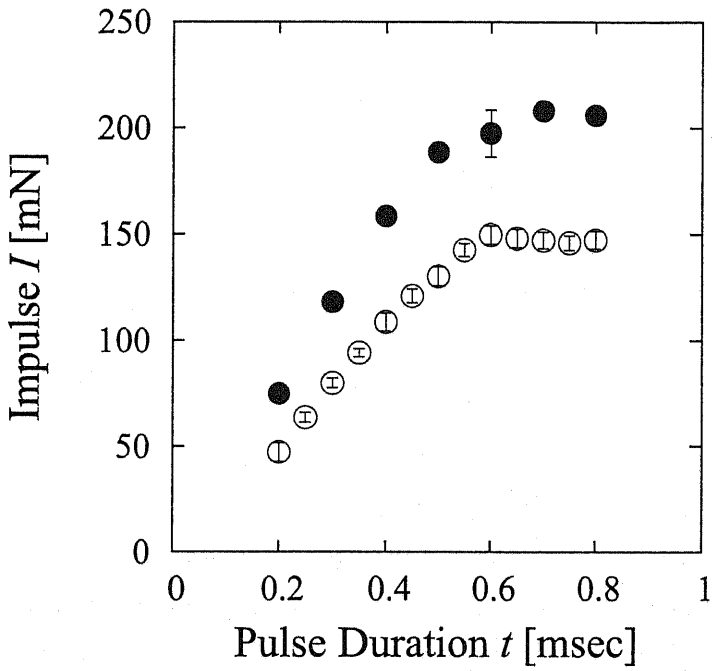

Figure 3.11: Dependence of Impulse I on the microwave pulse duration τ; o: from launch stage, •: in free space. ($S_{\mathrm{peak}} = 133\,\mathrm{kW/cm^2}$, $L = 380\,\mathrm{mm}$)

Figure 3.12 shows the pressure history with a damped oscillation during the refilling process. This oscillation is due to the air refilling process and pressure lower than ambient pressure in the thruster results in negative thrust I_{osc}.

$$I = \int (p - p_1) A dt = (p_4 - p_1) A t_{\mathrm{plateau}} + I_{\mathrm{osc}} \tag{3.12}$$

I_{osc} was deduced by integrating a damped oscillation history analytically approximated as follows;

$$I_{\mathrm{osc}} = \int_{\infty} A(p - p_1) dt = \int_{t_{\mathrm{plateau}}}^{\infty} -A(p_3 - p_1) e^{-\frac{t - t_{\mathrm{plateau}}}{\tau_{\mathrm{damp}}}} \sin\left(\frac{2\pi(t - t_{\mathrm{plateau}})}{\tau_{\mathrm{osc}}}\right) dt \tag{3.13}$$

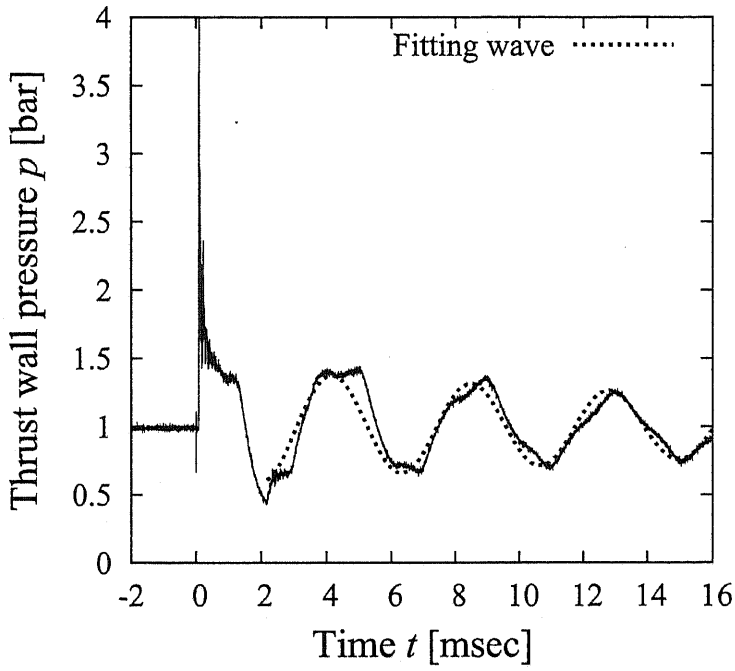

Figure 3.12: Pressure history at the thrust wall with pressure oscillation.

Executing integral in Eq.3.13,

$$= -A(p_3 - p_1)\frac{\frac{2\pi}{\tau_{\rm osc}}}{\left(\frac{1}{\tau_{\rm damp}}\right)^2 + \left(\frac{2\pi}{\tau_{\rm osc}}\right)^2} \tag{3.14}$$

Here, $\tau_{\rm damp}$ and $\tau_{\rm osc}$ are time constants of damping and oscillation period, respectively. Both time constants were deduced by curve fitting to the measured pressure history, and substituted into Eq.3.14.

Thrust impulse I was estimated with assumption of the negative thrust by air refilling process $I_{\rm osc}$ for various thruster length L. The relation of negative thrust by air refilling process to plateau thrust was deduced $I_{\rm osc}/I_{\rm plateau} = 0.75$ from measurement results.

Thrust impulse estimated from pressure history were plotted and compared with the result of the flight experiment of the thruster in free space in Fig.3.13. They showed a good agreement.

3.3.4 Thrust Performance and Plasma Traveling Length

The momentum coupling coefficient $C_{\rm m}$ was deduced from measured thrust. For discussion of a scaling law for the thruster design, a non-dimensional scale parameter l is defined as the ratio of the traveling length of the ionization front $L_{\rm plasma}$ to L. The value of $L_{\rm plasma}$ is a product of $U_{\rm ioniz}$ and pulse duration τ. Figure 3.15 shows the dependence of $C_{\rm m}$ on l. Figure 3.15 shows that an optimum length $l_{\rm opt}$ exists at 0.6-0.8.

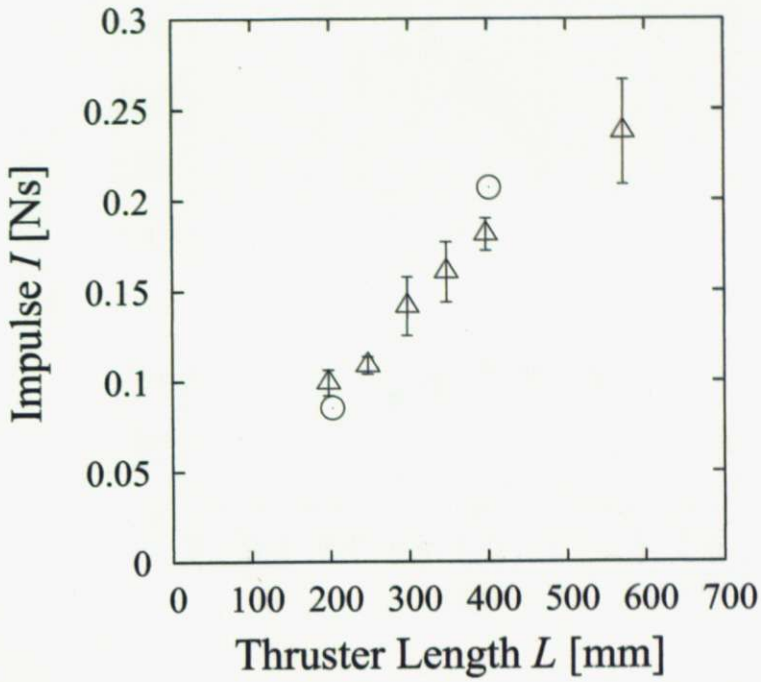

Figure 3.13: Comparison of impulsive thrust, thrust measurement result and estimation from pressure hisotry; ○: Result of flight experiment, △: Pressure measurement. ($S_{\mathrm{peak}} = 133\,\mathrm{kW/cm^2}$)

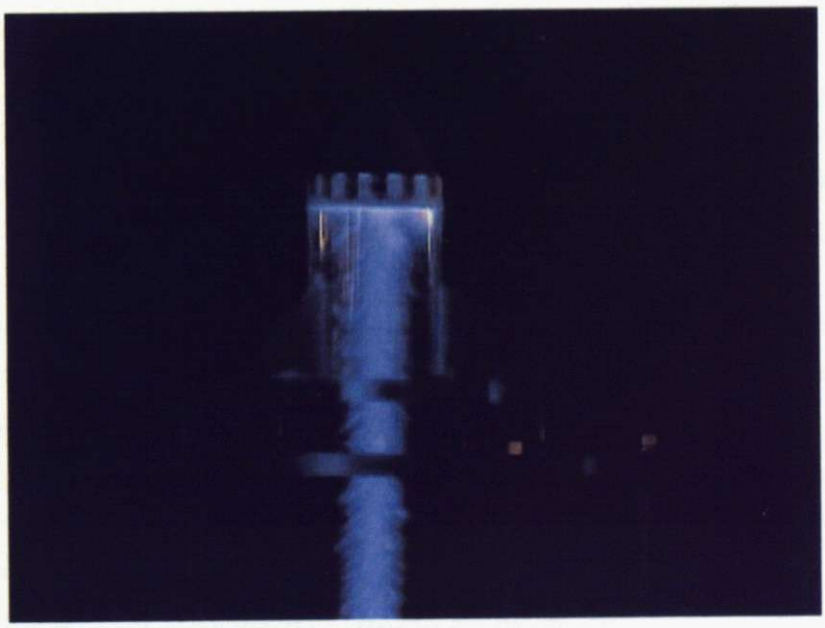

Figure 3.14: Photograph of plasma and cone-cylinder thruster model.

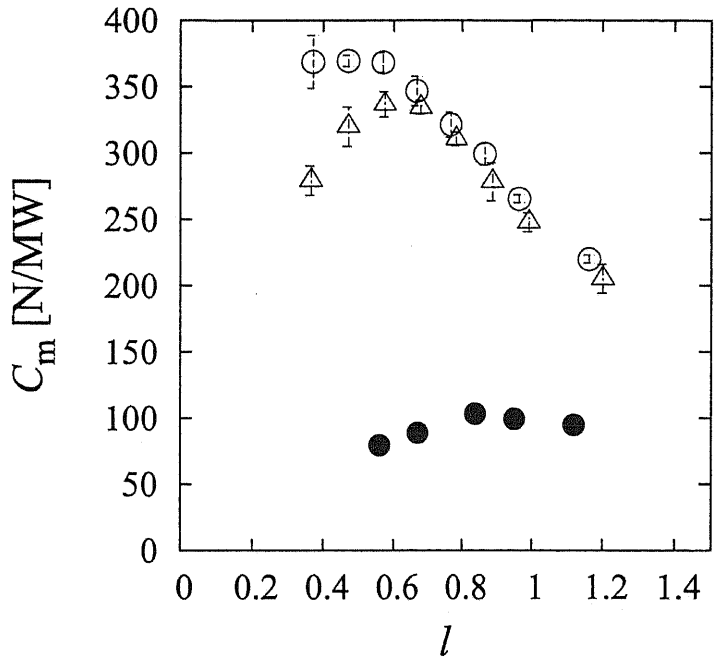

Figure 3.15: Dependence of momentum coupling coefficient C_m on normalized thruster length l; ○: $L = 380\,\mathrm{mm}$ thruster model at $S_{peak} = 98\,\mathrm{kW/cm^2}$, △: $L = 180\,\mathrm{mm}$ thruster model at $S_{peak} = 98\,\mathrm{kW/cm^2}$, ●: $L = 380\,\mathrm{mm}$ thruster model at $S_{peak} = 40\,\mathrm{kW/cm^2}$

As same, dependence of C_m on l was plotted for ϕ40mm thruster model(Fig.3.16) and the suspended thruster model(Fig.3.17) assuming the thruster in free space.

3.3.5 Thrust Performance and Microwave Power Density

In Fig.3.18, C_m at l_{opt} is portrayed as a function of M by changing the millimeter-wave power. When the ionization front propagates at a supersonic velocity, a shock wave forms at the ionization front and the post-shock pressure is enhanced through the heating process. As a result, high C_m was obtained at the $M > 1$ condition.

Theoretical thrust performance was calculated using the MSC energy conversion model. The dependence of C_m on the microwave power density was deduced. Dashed line indicates the calculation with assumption of negative thrust by air refilling process. The result was plotted with the result of the flight experiment on Fig.3.19. Figure 3.19 includes C_m of the thruster launched from the launch stage(○) and the suspended thruster (●). Estimated C_m showed good agreement with the result of thrust measurement in the free space(●) as same to the pressure history measurement.

On table 3.1, deduced C_ms using different methods are listed.

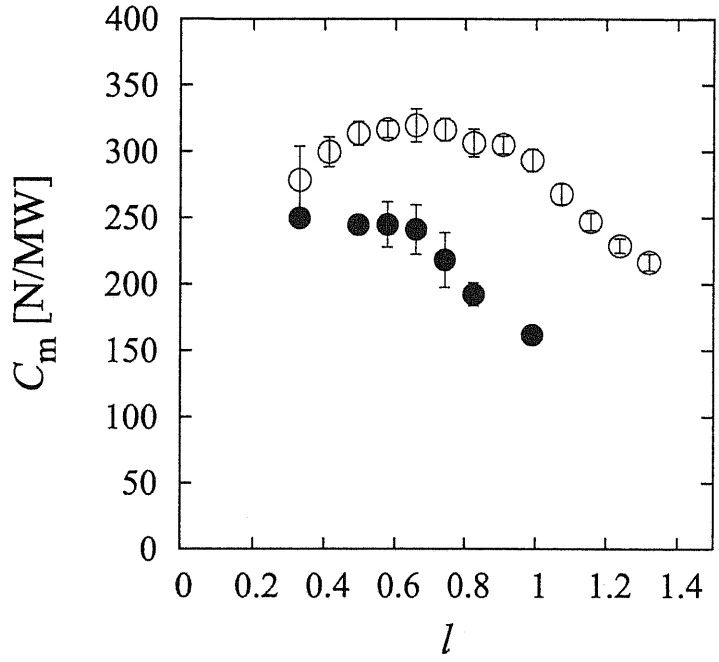

Figure 3.16: Dependence of C_m on the thruster diameter; ○: ϕ60mm thruster model, ●: ϕ40mm thruster model. ($S_{peak} = 133\,kW/cm^2$, $L = 380\,mm$)

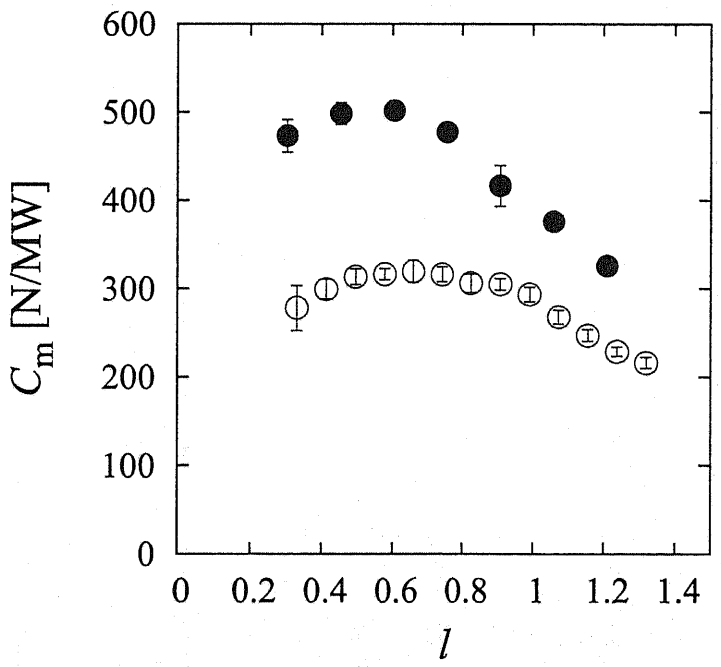

Figure 3.17: Dependence of C_m on the measurement condition; ○: from launch stage, ●: in free space. ($S_{peak} = 133\,kW/cm^2$, $L = 380\,mm$, $d = \phi 60\,mm$)

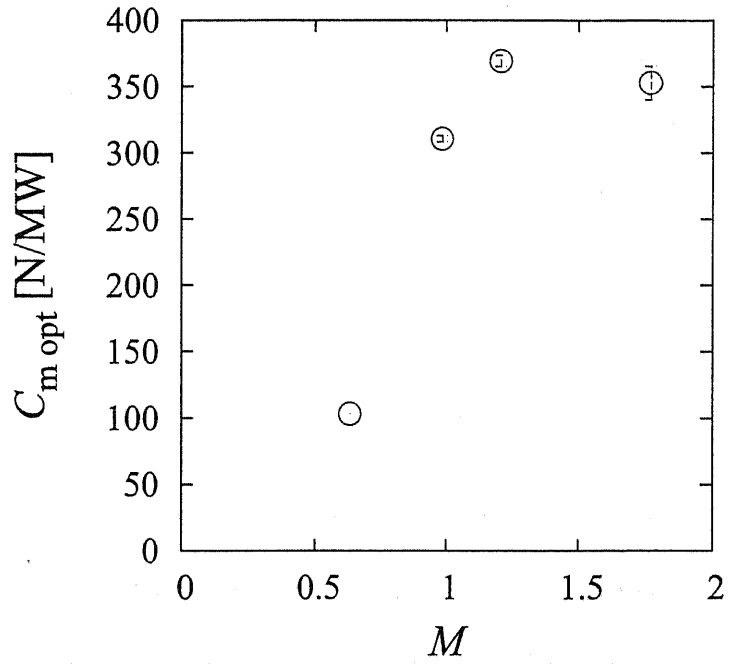

Figure 3.18: Dependence of momentum coupling coefficient C_m on mach number of Mach number of ionization front M

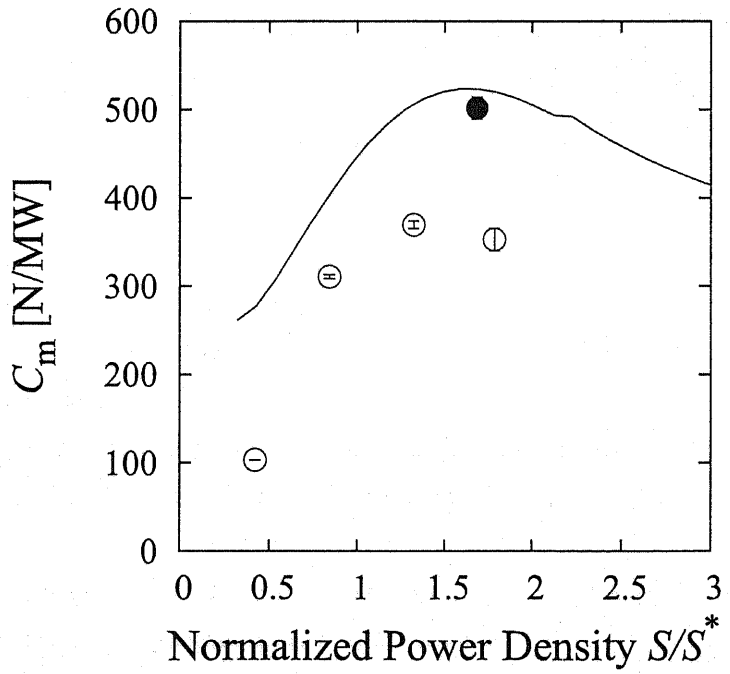

Figure 3.19: Comparison of momentum coupling coefficient C_m, measurement result and model calculation; ○: Results of thrusters launched from the launch stage, ●: Results of the hanged thruster, —: MSC cycle model calculation.

Table 3.1: Comparison of C_m

Thruster model	ϕ60 mm	ϕ40 mm
$\eta_{coupling}$	0.48	0.24
Measured C_m	320 N/MW	250N /MW
Measured C_m in free space	502 N/MW	-
Thrust generation cycle C_m	520 N/MW	290 N/MW

3.3.6 Comparison of Thrust Performance to Laser Propulsion

Through the exoerimental and analytical research on thrust generation cycle of Microwave Rocket, the maximum C_m was found up to 500 N/MW. The performance of BEPs are listed in table 3.2 for comparison.

As a result, C_m of Microwave Rocket is larger than the experimental results of laser propulsions. In addition, its C_m is larger than the necessary performance for launching estimated from the launch analysis.

Table 3.2: Comparison of C_m to laser propulsion

System	C_m	
Microwave Rocket	-500 N/MW	
Lightcraft Experiment Myrabo et al. (2000)[16]	-150 N/MW	Flight experiment using 10 kW CO_2 Laser
LITA Experiment Sasoh et al. (2003)[32]	290 N/MW	Xe
Launch analisys of Laser/Microwave Propulsion Katsurayama et al. (2004)[27]	300-50 N/MW	Beam:100-1000 MW Payload:10-100 kg
Launch analisys of Laser Propulsion Schall et al. (2000)[33]	275/300 N/MW	Beam:10 MW Payload:50 kg

3.4 Conclusion

Impulsive thrust force I was obtained using a thruster with a conical nose and a tube body with a high power millimeter wave beam.

Pressure at thrust wall was steady during the propagation of the shock and expansion waves in the thruster, same as the PDE's cycle. I estimated from the pressure history and obtained by the flight experiment was identical.

The value of C_m showed a peak at $l = 0.6 - 0.8$. High C_m was obtained at the high-power condition in which the ionization front propagates at supersonic velocity.

C_m dependence on the microwave power density calculated from the thrust generation cycle resembles the experimental result.

As a conclusion, the thrust generation cycle is thought to be appropriately expressing the physical

processes in Microwave Rocket, and would be useful for the design optimization of Microwave Rocket.

Chapter 4

Thrust Performance of Repetitive Pulse Operation and Air Refilling Process

To observe the effect of the forced breathing system, the dependence of velocities of the shock wave and the ionization front in the thruster was measured.

4.1 Definition of Partial Filling Rate

During the pulse interval, the air in the thruster is partially replaced by a forced breathing system. The fresh air provided from the thrust wall replaces the hot air remained in the thruster. The fractional rate of the fresh air filling in the thruster by forced breathing depends on the parameters, the thruster length L, the pulse repetition frequency f, the bulk velocity of forced air flow in the thruster u. Thus partial filling rate of forced breathing is defined as

$$\frac{\text{Fresh air volume}}{\text{Thruster volume}} = \frac{Au/f}{LA} = \frac{u}{Lf} \tag{4.1}$$

In the forced breathing system, weighted mean properties in the thruster express representing properties of the initial condition of the cycle. At the pulse repetition condition, temperature at hot remained air in the thruster is equal to the temperature of the exhausted air.

4.2 Experimental Setup and Measurement Apparatus

4.2.1 Multi Pulse Operation of Gyrotron

In the gyrotron, a milliemeter wave beam is oscillated through the interaction between the accelerated electron beams and the electromagnetic waves by a cyclotron resonance maser in a cavity with magnetic fields. In this study, to provide microwave pulses repetitively, the acceleration voltage of an electron beam was modulated and the oscillation mode in the cavity was controlled. The interval time duration between

pulses was settled 20 ms to 50 ms. The typical power history is shown in Fig.4.1. The pulse duration τ and peak power P of each pulse were about 1.7 ms or 3.4 ms and 270 kW, respectively.

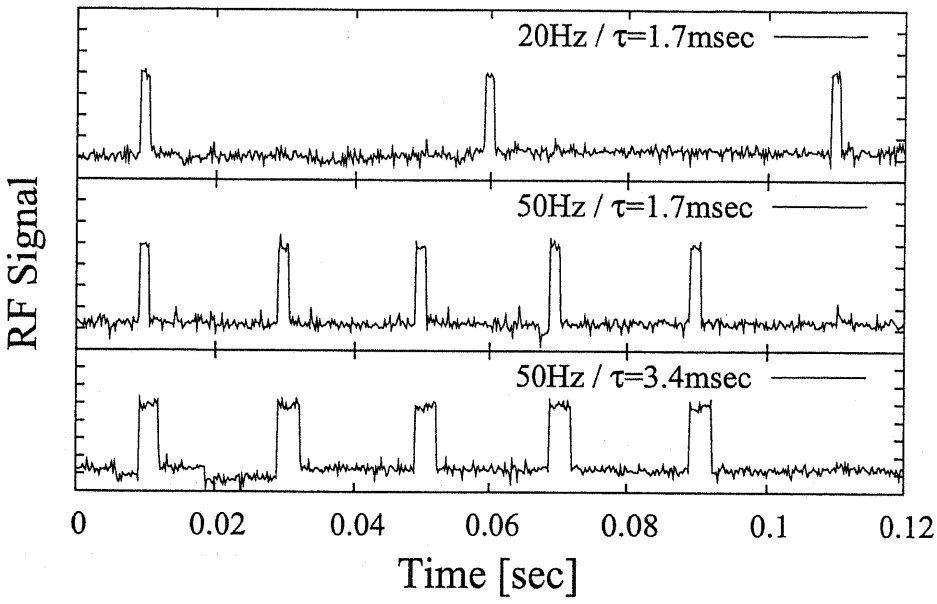

Figure 4.1: Typical record of microwave pulse history. $P = 270$ kW

A millimeter wave beam is transmitted through a corrugated waveguide to the experiment site. The output microwave beam was a fundamental Gaussian beam with a 20 mm waist.

4.2.2 A Thruster Model with Forced Breathing System

A conceptual thruster model composed of a cylindrical tube with a conical nose was used as shown in Fig.4.2. A shock wave and an ionization front propagate through the cylindrical tube absorbing the millimeter wave beam during the pulse. The total length of the thruster was variable from 190 mm to 590 mm. The tube diameter was 60 mm.

The fresh air is supplied from the thruster wall. Four flexible tubes were connected to the conical nose and a high pressure tank. Four electric controlled valves (AB41-03-4; CKD) controlled the air flow in the each tube. The flow velocity of the fresh air in the thruster was controlled by the number of valves to control. Pressure at a high pressure tank was kept 0.4 MPa using a pressure regulator. The designed flow velocity u was varied from 2.5 m/s to 10 m/s.

As the speed of fresh air flow in the thruster by forced breathing is lower than the shock wave, the velocity had small dependency on the u.

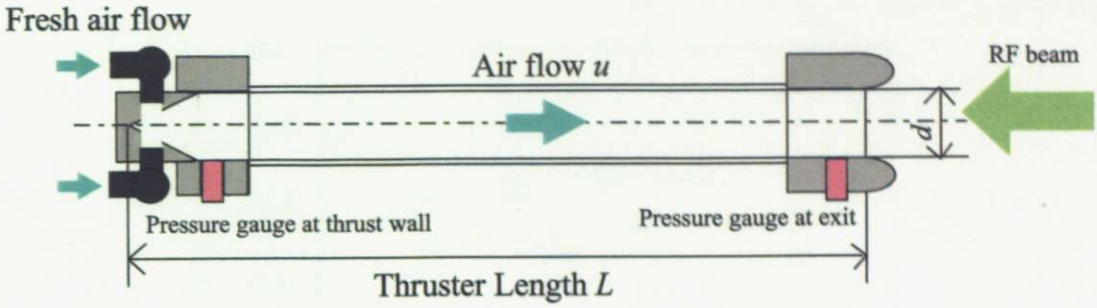

Figure 4.2: Schematics of a thruster model with forced breathing system and pressure measurement gauges.

4.2.3 Shock Wave Observation

Two pressure gauges (603B; Kistler) were mounted at the cylindrical tube and measurement pressure histories in the thruster to deduce the average velocity of a shock wave as shown in Fig.4.2. One is settled near the thrust wall and another is settled near the exit. The average velocity of the shock wave in the thruster was deduced from the difference of the arrival time of the shock wave at each gauge.

4.2.4 Continuous Thrust Observation

The thruster model with force breathing system was settled on the stand with the movable linear guide and it start a linear movement by thrust force. The trajectory of the head of the thruster was measured using a laser displacement gauge. The motion was constrain in 100 mm because flex tubes can track the thruster. The mass of thruster model m was 2.2 kg.

4.3 Experimental Result and Discussion

4.3.1 Thrust Impulse of Force Breathing System

The pressure history in the thruster under the multi pulse operation was measured. The operation of the pulse repetition at 20 Hz to 50 Hz was carried out for around 0.1 s duration. During the operation, 3 to 5 pulses were provided to the thruster. At each pulse, the shock wave was observed in the thruster. The propagation velocities of a shock wave observed at each pulse input are plotted on Fig.4.3 and the thrust impulses are plotted on Fig.4.4. When the first pulse is inputted at $t = 0$ s, the propagation velocity of the shock wave was identical to the result of the single pulse operation. After the second pulse, the propagation velocity was increased and the propagation velocity was steady for latter pulses. Therefore after the third pulse the operation is expected to be steady. The propagation velocity U at multi pulse operation was defined the average of the velocities obtained after the third pulse.

As the same to the propagation velocity of the shock wave, thrust impulse imparted at each pulse has the same dependence. The impulse decreased at the second pulse and the steady impulse was also

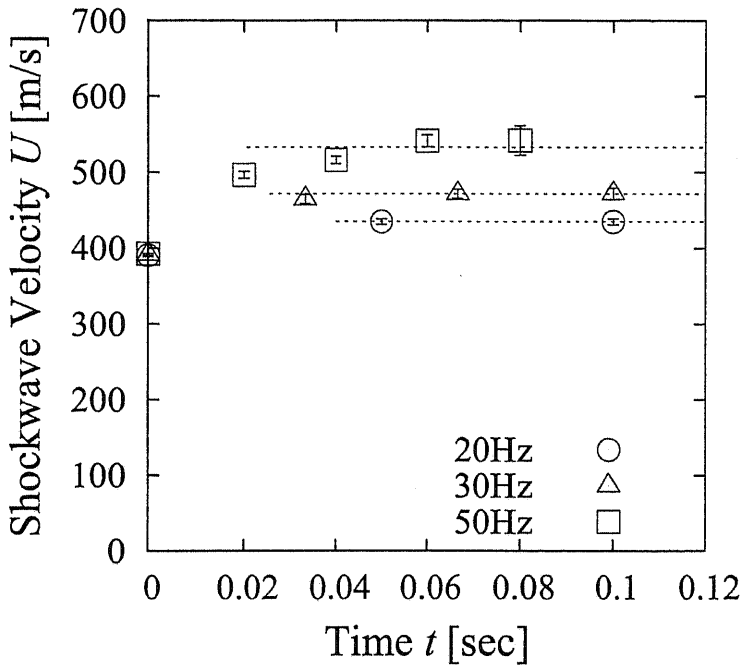

Figure 4.3: Shock wave velocity $U_{\mathbf{shock}}$ imparted by each pulse using 290mm thruster model; ○: 20Hz; △: 30Hz; □: 50Hz.

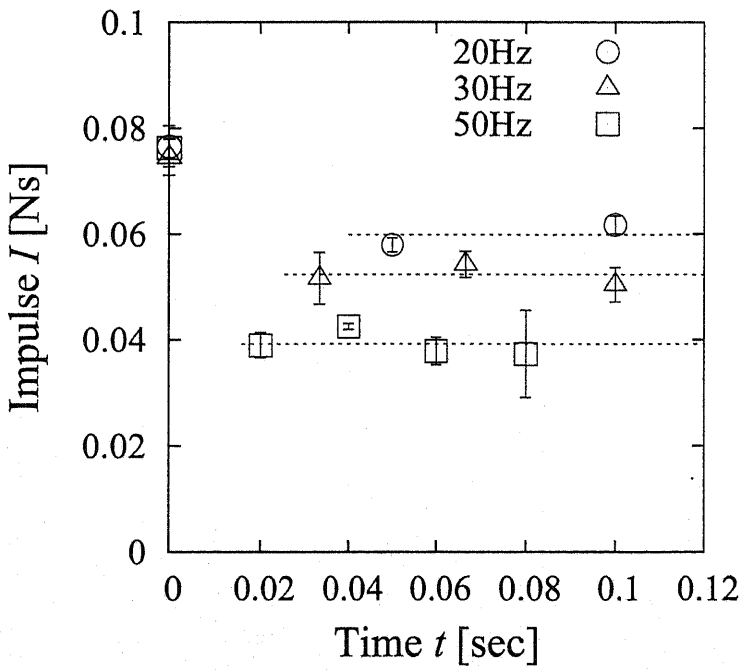

Figure 4.4: Impulse I imparted by each pulse using 290mm thruster model; ○: 20Hz; △: 30Hz; □: 50Hz.

obtained at latter pulses. At the steady operation, the average of the thrust impulses obtained at latter pulses was defined as impulse I at the multi pulse operation.

Finally pressure histories under the repetitive pulse operation for 1sec duration were measured. The repetition frequency was settled 20 Hz and 50 Hz. Figure 4.5 and 4.6 shows the result of 50 Hz and 20 Hz repetition, respectively. As shown, the shock wave is formed at each pulse and the thrust impulse is generated. Thrust performance is listed on Table 4.1.

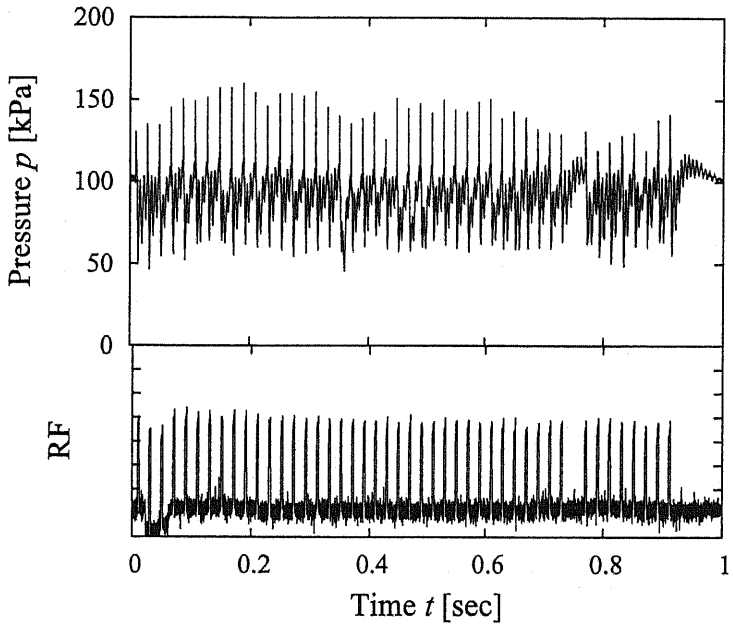

Figure 4.5: Pressure and RF history at $f = 50$ Hz.

Table 4.1: Thrust performance under 1s steady operation.

Frequency f	Impulse I	Thrust F	C_{m}
50Hz	0.07 Ns	3.5 N	79 N/MW
20Hz	0.14 Ns	2.7 N	151 N/MW

Thrust impulses estimated from pressure history are plotted on Fig.4.7. The thrust impulse is smaller than impulse at the first pulse and thrust impulse becomes steady at latter pulses. As a result, the steady operation is achieved in both frequencies.

4.3.2 Dependence of Thrust Performance on Partial Filling Rate

To validate the model, the average propagation velocity of the shock wave and the impulse were measured for various conditions. The condition of the air flow velocity were $u = 2.5\,\mathrm{m/s}$ for the thruster length

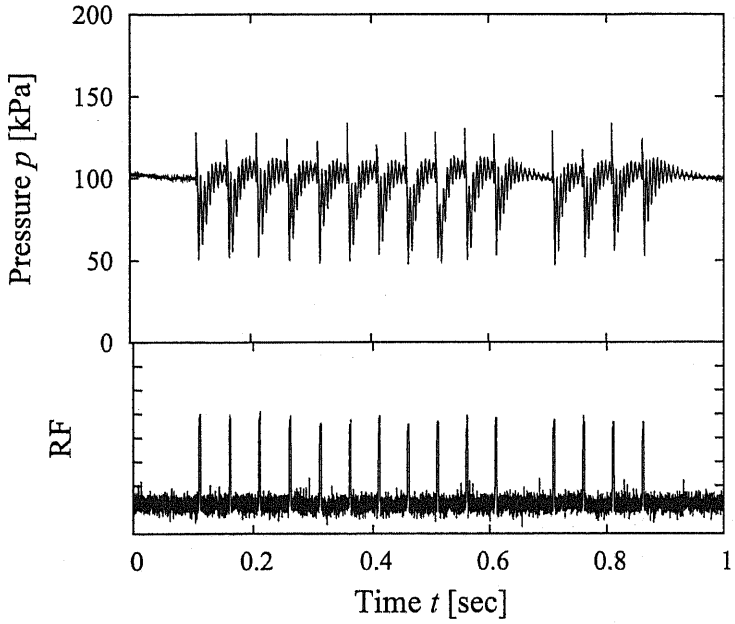

Figure 4.6: Pressure and RF history at $f = 20$ Hz.

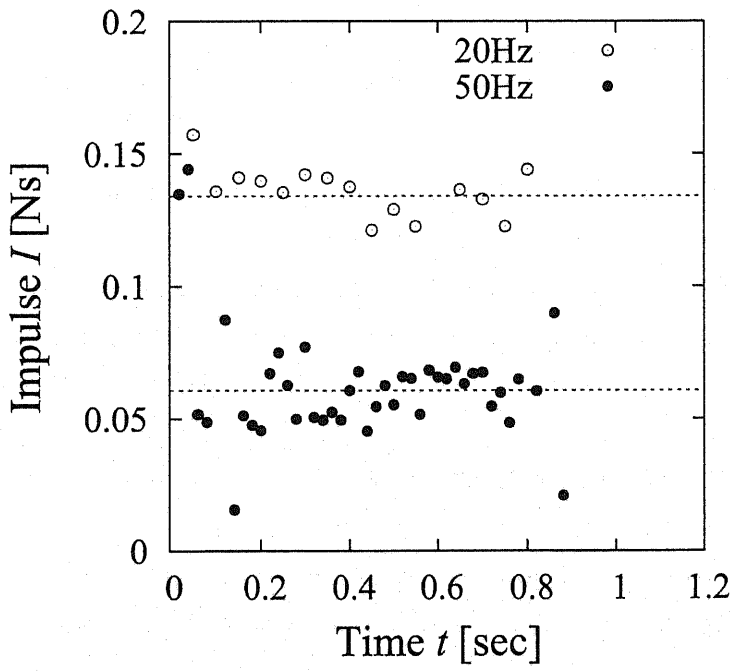

Figure 4.7: Impulse I imparted by each pulse at 50Hz/1s operation: ○: 20Hz; ●: 50Hz.

$L = 190 - 490\,\mathrm{mm}$, and $u = 10\,\mathrm{m/s}$ for the thruster length $L = 390\,\mathrm{mm}$. Figure 4.8 shows the dependence of the propagation velocity of the shock wave on the partial filling rate. As shown, the experimental results on the propagation velocity showed good agreement to the predicted dependence by the thrust generation model based on the normal shock wave driven by atmospheric plasma under partial filling condition.

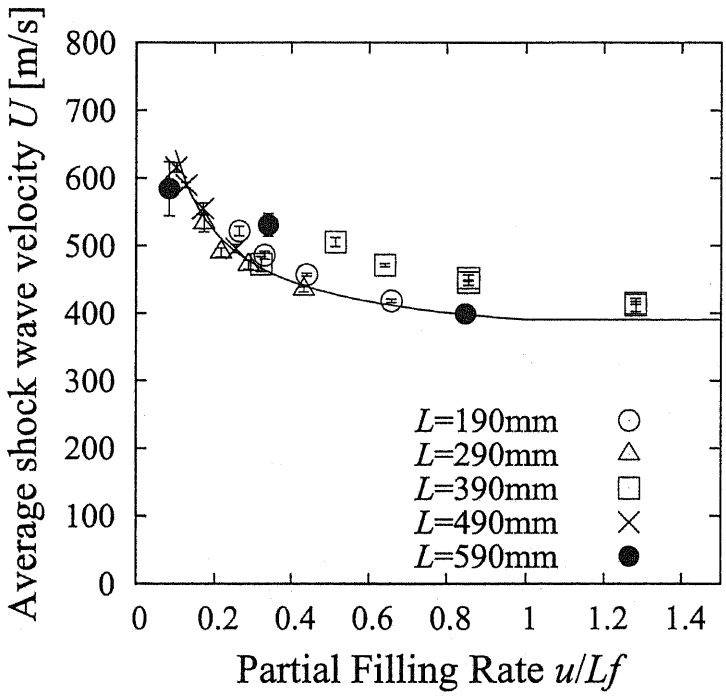

Figure 4.8: Dependence of average propagation velocity of the shock wave on partial filling rate; ○: L=190 mm thruster; △: L=290 mm thruster; □: L=390 mm thruster; ×; L=490mm thruster; • L=590 mm thruster; −: MSC cycle model calculation.

To compare the dependency of the thrust performance on the partial filling rate for difference thruster length, the normalized thrust impulse was deduced because the thrust impulse obtained at each cycle depends on the thruster length. Normalized impulse I/I_{single} was defined as the ratio of the average impulse at the multi pulse operation to that at the single pulse operation. Figure 4.9 shows the dependence of the normalized impulse on the partial filling rate and the thruster length. In the graph, the partial filling rate u/Lf was used for the horizontal-axis.

As shown in Fig.4.9, the experimental result on the thrust impulse showed good agreement to the predicted dependence as same to the shock wave.

Finally, when the partial filling rate becomes unity, the normalized thrust impulse I/I_{single} become unity. This result indicates that the microwave rocket can be operated without performance degrease under enough filling process.

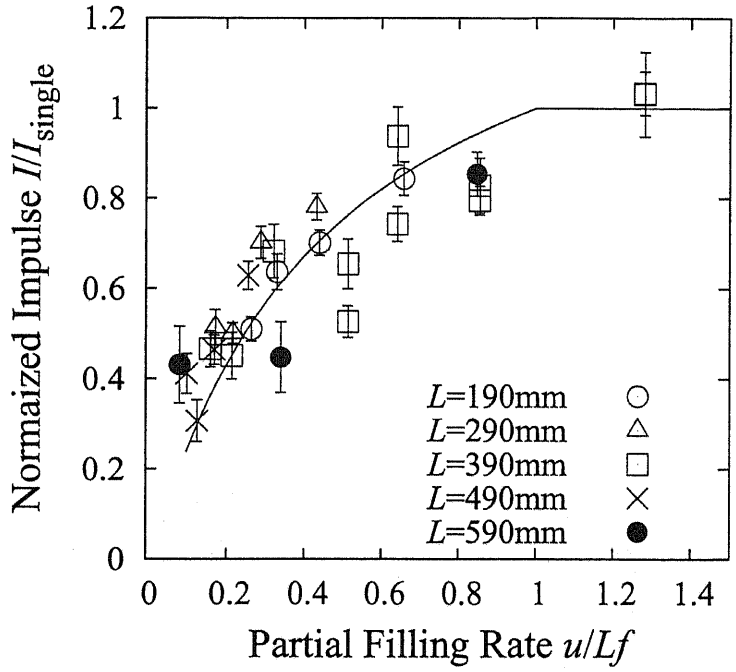

Figure 4.9: Dependence of normalized impulse I/I_{single} on partial filling rate; ○: L=190 mm thruster; △: L=290 mm thruster; □: L=390 mm thruster; ×; L=490mm thruster; • L=590 mm thruster; −: MSC cycle model calculation.

4.3.3 Thruster Motion and Total Impulse

The 1sec duration operation was conducted with thruster on the movable stand. The repetition frequency was 50Hz. Figure 4.10 shows the measurement result of the laser displacement gauge of the thruster head. As shown in Fig.4.10, the thruster moves at the constant acceleration motion. The trajectory of the thruster was analyzed with curve fitting and its acceleration was deduced. As a result, the acceleration was $a = 1.6\,\mathrm{m/s^2}$. From equation of motion and the mass of the thruster, thrust force worked for motion was estimated as $F = 3.4\,\mathrm{N}$. However the actual thrust was expected larger than this because the friction of the movable stand and drag from the air flex tubes were not assumed.

The thrust estimated from pressure history and trajectory was listed on Table 4.2. Both results show good agreement. As result, continuous thrust operation was demonstrated.

Table 4.2: Comaparison of results of pressure history measurement and trajectory measurement under 1s steady operation.

Measurement Method	Thrust Force F
Pressure History	3.5N
Trajectory	3.4N

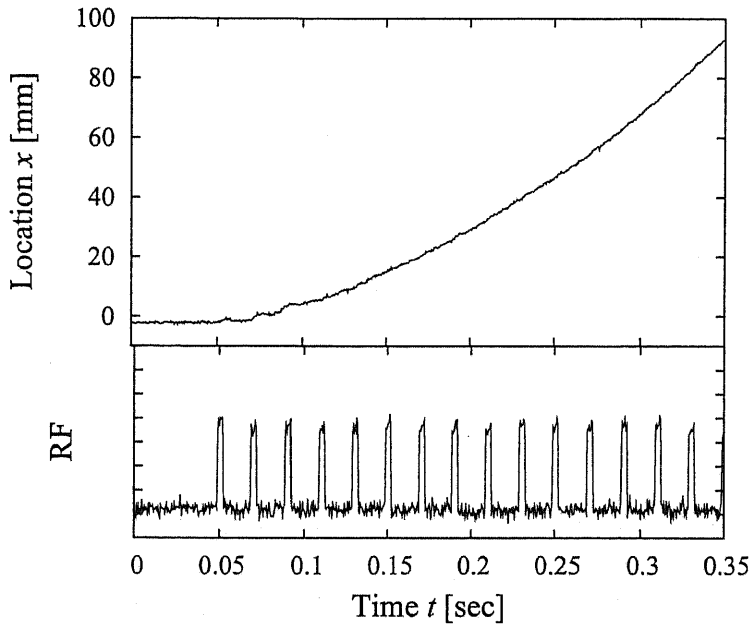

Figure 4.10: History of thruster trajectory and RF pulses, $f = 50$ Hz.

4.4 Conclusion

The propagation velocity of the shock wave at the multi pulse operation was increased from the result obtained at the single pulse operation. After the third pulse, the shock wave velocity measured at each pulse input was steady. As same, the impulse imparted by each pulse decreased from the result obtained at the single pulse operation. The steady repetitive operation was achieved after the third pulse.

The analytical thrust performance estimation based on the thrust generation model with the partial filling of the fresh air resembled experimental results. As a result, the thrust performance was identical to the thrust at the single pulse operation when the partial filling rate is unity.

This result shows that the Microwave Rocket can be operated without any performance decrease with perfect air-filling.

Chapter 5

Thrust Performance in Reduced Ambient Pressure

5.1 Plasma Structure and Ambient Pressure

Plasma formed in the millimeter wave beam has a unique structure. Because the wave length is smaller than the beam, the interference of waves is easily observed and affects on plasma structure. And because the frequency is at the same order to the collision frequency of neutral particles of air, the phenomena would have strong dependence on the ambient pressure condition.

Vikharev et al. observed structure of plasma in the high power millimeter wave beam. They found three types of the structure depending gas pressure, (1) continuous plasma at low pressure, (2) plasma strips coaxial to the beam at moderate pressure, and (3) plasma filaments perpendicular to the beam (a fish-bone structure) at high pressure. The pressure threshold of changing the discharge structure had dependence on gas species.

Hidaka et al. observed and simulated structure formation of the atmospheric millimeter wave plasma. They pointed out that the array has two-dimensional structure which resembled the profile of the millimeter wave diffracting around the plasma column.

5.2 Experimental Setup and Measurement Apparatus

5.2.1 Chamber for Reduced Ambient Pressure Condition

Experiments were carried out under the ambient pressure of 0.1-1 atm using a cubic chamber with a 30 cm side. (Figs.5.1 and 5.2) The chamber had optical windows on the top and side for observation. The chamber pressure was measured by a crystal pressure gauge (Crystal Gauge M-320XG; Anelva Co. Ltd.). The millimeter wave beam was launched into chamber from the bottom of it.

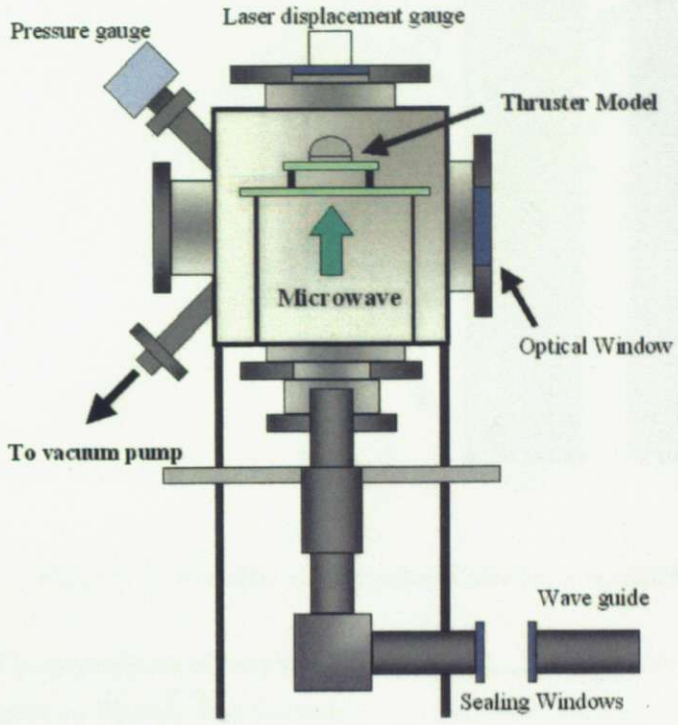

Figure 5.1: Schematic of a chamber setup

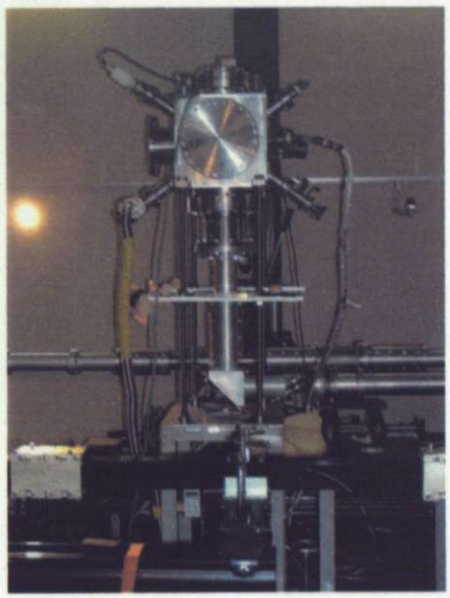

Figure 5.2: Photograph of reduced pressure chamber

5.2.2 Parabolic Thruster Model and Thrust Measurement

A thruster model has a parabolic reflector whose diameter and focal length are 90mm and 15mm, respectively. It is made of duralumin and weighs 100g. Impulsive thrust was estimated from the flight altitude of the model measured using a laser displacement gauge(LB-02; Keyence Co. Ltd.) through the chamber top window.

5.2.3 Plasma Observation

Pictures of plasma glow toward millimeter wave beam source were taken using a high-speed framing camera(FASTCAM Ultima 40K; Photoron Co. Ltd.) through an optical window on the chamber side as shown in Fig.5.1. The framing speed was 40,500 frames/s. The propagation velocity of ionization front was estimated using a series of these pictures.

5.3 Experimental Result and Discussion

5.3.1 Propagation Velocity of Ionization Front

Figure 5.3 shows pictures of 170GHz millimeter wave breakdown taken using the fast framing camera under various ambient pressure conditions. The ionization front of plasma propagated in constant velocity. Using the series of pictures, the ionization front velocity was estimated.

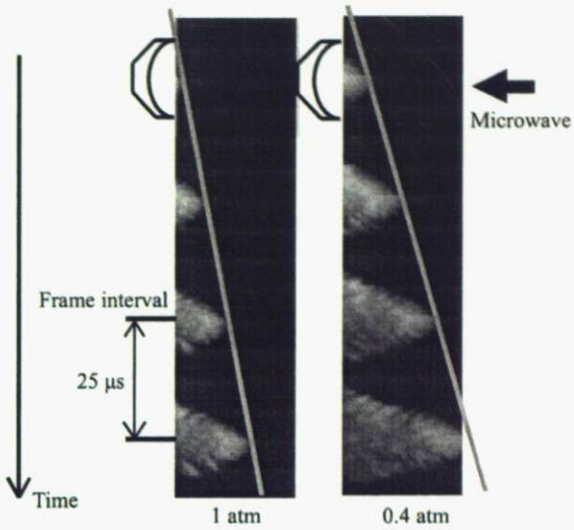

Figure 5.3: Framing photographs of plasma propagation under reduced pressure condition.

The dependence of propagation velocity U_{ioniz} of the ionization front on millimeter wave power density S shows on Fig.5.4. The horizontal axis indicates normalized millimeter wave power density S/S^* which is defined as the ratio of the millimeter wave power density when its propagation velocity of the ionization front becomes sonic speed ($a = 331m/s$) at atmospheric pressure $p = 1\,\text{atm}$. U_{ioniz} increases with S increment.

Figure 5.5 shows the dependence of propagation velocity U_{ioniz} on ambient pressure. With decrease of ambient pressure, propagation velocity of ionization front increases. In all the measurement condition, temperature of air in the chamber was same and the sonic speed was same. Therefore Mach number of the ionization front was increased with ambient pressure decrease.

5.3.2 Dependence of Plasma Structure on Ambient Pressure

With change of ambient pressure, the structure of plasma was changed. Figure 5.6 shows the photographs of plasma structure taken by home movie camera. Figure 5.7 shows the photographs of plasma structure under various ambient pressure conditions taken by fast framing camera. When the ambient pressure was 1.0atm to 0.2 atm, small filament structure was observed. Indeed when smaller than 0.15 atm, small structure was disappeared and continuous plasma was observed.

The dependence of structure is related to the energy absorption scale. When air density is decreased energy absorption scale becomes far larger than filament size and the structure is not supported.

According to Vikharev et al., the threshold pressure of the plasma structure change was 0.005 atm. Comparing the result, threshold pressure has dependence on frequency and gas species.

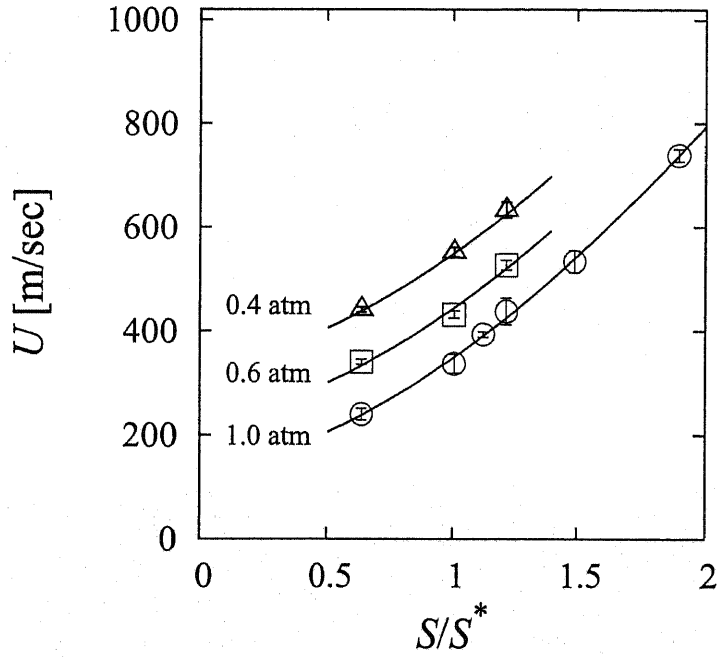

Figure 5.4: Dependence of propagation velocity of the ionization front U_{ioniz} on normalized power density S/S^*; ○: p_1=1.0 atm; △: p_1=0.6 atm; □: p_1=0.4 atm.

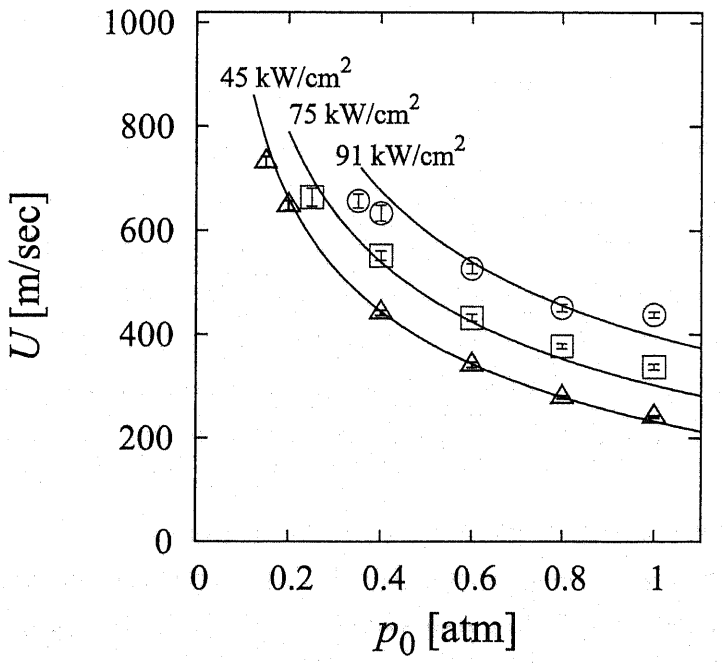

Figure 5.5: Dependence of propagation velocity of the ionization front U_{ioniz} on ambient pressure p_1; ○: S=91 kW/cm^2; △: S=75 kW/cm^2; □: S=45 kW/cm^2.

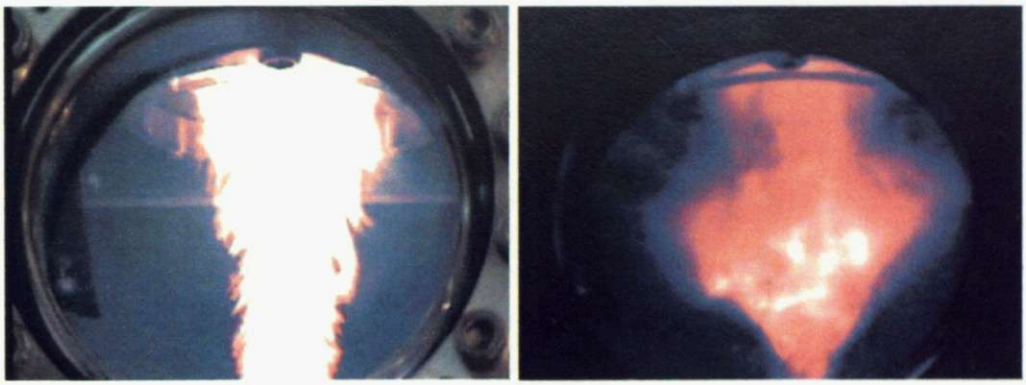

p=1.0 (atm) p=0.1 (atm)

Figure 5.6: Photographs of plasma structure on the beam in reduced ambient pressure. 170GHz

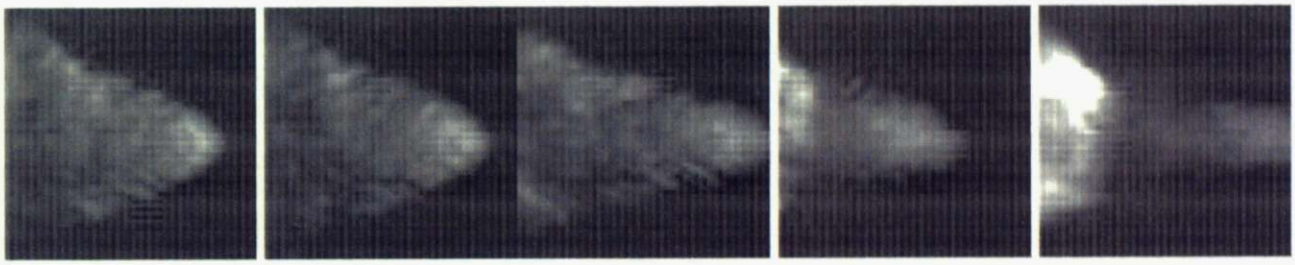

p_1=1.0 (atm) p_1=0.8 (atm) p_1=0.4 (atm) p_1=0.2 (atm) p_1=0.15 (atm)

Figure 5.7: Photographs of plasma structure under reduced conditions. 170GHz, P=312kW, Exposure time: 25μs

5.3.3 Thrust Performance and Ambient Pressure

Thrust impulse was measured using a parabolic thruster under 0.1 to 1.0 atm ambient pressure condition. The parabolic thruster was launched vertically and its flight trajectories were recorded. Input millimeter wave power was $P = 595\,\mathrm{kW}$. As a result, the flight trajectories of the thruster was obtained under 1.0 to 0.2 atm condition and momentum coupling coefficient C_m was deduced. Indeed thrust impulse under 0.1 atm was too small to detect. The measurement result was plotted in Fig.5.8.

Because thrust performance depends on microwave pulse duration τ and the ionization front velocity U_ioniz, coupling coefficient was plotted for the normalized thruster length $l = U_\mathrm{ioniz}\tau/L$. U_ioniz was applied the result obtained in last section.

As shown in Fig.5.5, because U_ioniz increases with p_1 decrease, the optimum C_m is obtained with short pulse duration τ in low ambient pressure. At the optimum pulse duration condition, C_m was nearly constant to ambient pressure. This is because the shock wave under low ambient pressure has large Mach number with large pressure increment. Then pressure at thrust wall was constant to ambient pressure and C_m was constant.

Indeed thrust impulse decreased under 0.1 atm. Under 0.1 atm, as shown in last section, the structure

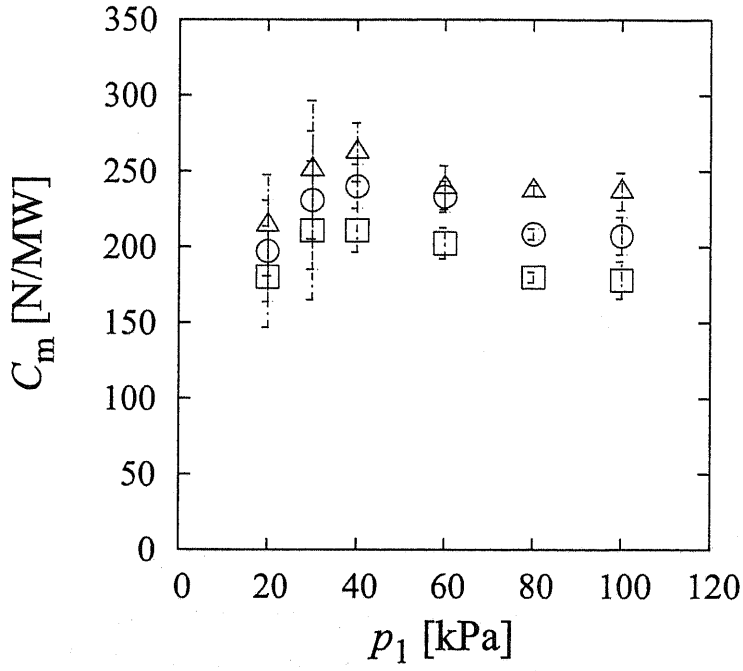

Figure 5.8: Dependence of momentum coupling coefficient C_m on ambient pressure p_1; △: l=2.0; ○: l=3.0; □: l=4.0.

of plasma was changed and the relation of shock wave and ionization front would be changed far from that of the atmospheric condition.

5.4 Conclusion

With decrease of ambient pressure p_1, propagation velocity of ionization front U_{ioniz} increases. With change of ambient pressure p_1, the structure of plasma was changed. When the ambient pressure was 1.0atm to 0.2 atm, small plasma filaments were observed. Indeed when smaller than 0.1 atm, the structure was disappeared and continuous plasma was observed.

Because U_{ioniz} increases with p_1 decrease, the optimum C_m is obtained with short pulse duration τ in low ambient pressure. At the optimum pulse duration condition, C_m was nearly constant to ambient pressure. Indeed thrust impulse decreased under 0.1 atm.

Chapter 6

Design of Microwave Rocket

Relations of each conclusion for the design for Microwave Rocket are explained in Fig.6.1. Figure 6.1 shows the relations of conclusions of this study to the design of Microwave Rocket.

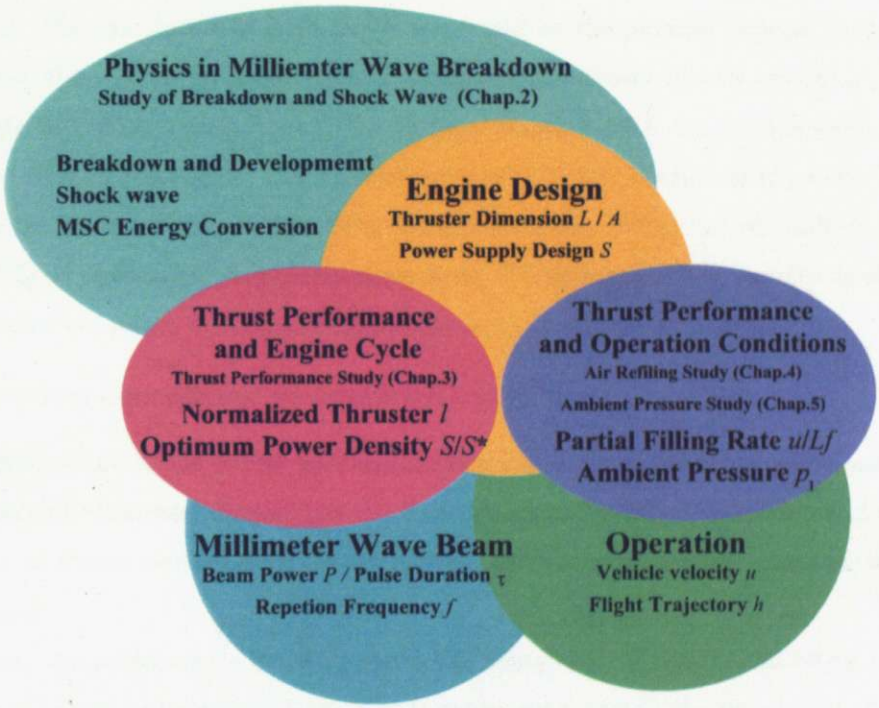

Figure 6.1: Relations for Microwave Rocket Design.

Engine design

The engine design of Microwave Rocket would be ruled by the design guideline for the optimum dimensions of the thruster length L and area of thrust wall A and the profile and power density S of microwave in the thruster, which is controlled by the beam converter. And its performance is predictable by the engine cycle and energy conversion models.

Beam generators

The microwave beam generator is required to provide necessary power P, pulse duration τ and repetition frequency f for thrust generation. The power condition is designed from the thrust performance of the engine, which is calculated from the engine cycle.

Operation and flight conditions

The control sequence of Microwave Rocket during the launch is also provided from the result of this thesis. The performance dependence on the intake flow velocity of vehicle speed u and the ambient pressure of flight altitude p is predictable from the thrust generation cycle model. Therefore it is possible to design the flight trajectory and control sequence of the Microwave Rocket launch system.

Thrust performance and engine cycle

The thrust generation cycle of Microwave Rocket based on the MSC energy conversion process was discussed in Chap.3. The calculation of cycle model was based on the physical process discussed in Chap.2.

As conclusions, there is the optimum thruster length for a microwave pulse condition. When the ratio of traveling length of the ionization front to the thruster length l is 0.6, C_{m} is maximum. l is determined from L, the dimension of the engine, and τ, microwave pulse pulse duration of the beam generator

There is also the optimum microwave power density condition. When the normalized power density is $S/S^{*} = 1 \sim 2$, C_{m} is optimized. It is determined from S microwave power density in the engine which related to P, microwave power of the beam generator, and A, area of the engine.

Thrust performance dependence on operation condition

Although the basic result of the thrust generation cycle and design policy was discussed in Chap.3, the thrust performance of Microwave Rocket has also dependence on operation condition and its environment. The dependence of thrust performance on air refilling process and ambient pressure was discussed in Chap.4 and Chap.5.

As conclusions, the performance depends on partial filling rate. When partial filling rate is unity, the maximum C_{m} is obtained. The partial filling rate is determined from u, the flow speed of the vehicle's air intake, L, the engine length, and f the repetition frequency of the beam generator.

The performance also depends on ambient pressure. When ambient pressure is larger than $p_1 > 0.1$ atm, the thrust performance is nearly same to that at $p_1 = 1.0$ atm condition. p is determined from flight alitude during the launch seaquence.

Using these relations of the thrust performance of Microwave Rocket, the design of Microwave Rocket can be developed.

Study of breakdown and shock wave

Guidelines for optimumized engine design are determined by the engine cycle. The engine cycle is based on the physical phenomena. The physical phenomena on the millimeter wave breakdown were discussed in Chap.2.

The propagation velocity of the ionization front of millimeter wave atmospheric plasma was measured. The propagation velocity becomes supersonic when $S > 75\,\mathrm{kW/cm^2}\,(= S^*)$ The propagation velocity of the shock wave was also measured and compared to that of the ionization front. The both velocity was identical to each other when U_{ioniz} is supersonic.

Using the results of the propagation velocities, the energy conversion model of millimeter breakdown and its shock wave driving was discussed. The MSC energy conversion model resembled the experimental result.

This energy conversion model is important for the development of the thrust generation model for Microwave Rocket and it design method.

Chapter 7

Conclusion

7.1 Millimeter wave Breakdown and its Energy Conversion

A millimeter wave discharge was ignited in the atmosphere by focusing a millimeter-wave beam with a parabolic reflector at the focal point.

The propagation velocity of the ionization front increased with the millimeter wave power density. It became supersonic at power densities greater than $75\,\mathrm{kW/cm^2}$. The dependence of velocity was identical in free space and in-tube condition.

The ionization front and the shock wave propagated in nearly constant velocity in the tube. When the ionization front propagated at supersonic speed, both velocities were identical.

The MSC model estimation of post-shock wave pressure and sonic speed using estimated η_{coupling} resembled measurement result.

7.2 Thrust Performance of Microwave Rocket

Impulsive thrust force I was obtained using a thruster with a conical nose and a tube body with a high power millimeter wave beam.

Pressure at thrust wall was steady during the propagation of the shock and expansion waves in the thruster, same as the PDE's cycle. I estimated from the pressure history and obtained by the flight experiment was identical.

The value of C_{m} showed a peak at $l = 0.6 - 0.8$. High C_{m} was obtained at the high-power condition in which the ionization front propagates at supersonic velocity.

C_{m} dependence on the microwave power density calculated from the thrust generation cycle resembles the experimental result.

7.3 Continuous Thrust Performance and Air Refilling Process

The propagation velocity of the shock wave at the multi pulse operation was increased from the result obtained at the single pulse operation. After the third pulse, the shock wave velocity measured at each pulse input was steady. As same, the impulse imparted by each pulse decreased from the result obtained at the single pulse operation. The steady repetitive operation was achieved after the third pulse.

The analytical thrust performance estimation based on the thrust generation model with the partial filling of the fresh air resembled experimental results. As a result, the thrust performance was identical to the thrust at the single pulse operation when the partial filling rate is unity.

7.4 Thrust Performance and Ambient Pressure

With decrease of ambient pressure p_1, propagation velocity of ionization front U_{ioniz} increases. With change of ambient pressure p_1, the structure of plasma was changed. When the ambient pressure was 1.0atm to 0.2 atm, small filament like structure was observed. Indeed when smaller than 0.1 atm, small structure was disappeared and bulk plasma was observed.

Because U_{ioniz} increases with p_1 decrease, the optimum C_{m} is obtained with short pulse duration τ in low ambient pressure. At the optimum pulse duration condition, C_{m} was nearly constant to ambient pressure. Indeed thrust impulse decreased under 0.1 atm.

7.5 Design of Microwave Rocket

The design guideline for Microwave Rocket was showed as relations of following design parameters; L, the thruster length of the engine, A, the thrust wall area of the engine, P, power of the microwave beam generator, τ the pulse duration of the generator, f, the repetition frequency of the generator, u, flow speed in the air intake of the engine at the flight condition, and p, ambient pressure at the flight condition. These parameters are related to each other and convert to following parameters which determin thrust performance C_{m}; l, normalized plasma length, S, microwave power density, and partial filling rate.

Bibliography

[1] A.V. Gaponov-Grekhov and V.L. Granatstein, editors. *Applications of High-Power Microwaves*, pages 1–24. Artech House, INC, 1994.

[2] M. Thumm. Progress in gyrotron development. *Fusion Engineering and Design*, 66:69–90, 2003.

[3] K. Sakamoto, A. Kasugai, K. Takahashi, R. Minami, N. Kobayashi, and K. Kajiwara. Achievement of robust high-efficiency 1mw oscillation in the hard-self-exitation region by a 170ghz continuous-wave gyrotron. *Nature Physics*, 3(6):411–414, 2007.

[4] A. Kasugai, K. Sakamoto, R. Minami, K. Takahashi, and T. Imai. Study of millimeter wave high-power gyrotron for long pulse operation. *Nuclear Instrument and Method in Physics Research A*, 528:110–114, 2004.

[5] K. Sakamoto. Application of plasma heating technology for fronteir science. In Hideo Sugai, Kohnosuke Sato, and Akihiro Kono, editors, *Proceedings of Plasma Science Symposium 2005 and The 22nd Symposium on Plasma Processing*, pages 25–26. The Japan Society of Plasma Science and Nuclear Fusion Research, 2005.

[6] S.A.Brown. *Basic Data of Plasma Physics, 1966*, pages 251–255. The M.I.T. Press, 2nd edition, revised edition, 1967.

[7] Yu. P. Raizer. Propagation of high-pressure microwave discharege. *Soviet Physics JETP*, 34(1):114–120, January 1972.

[8] Yu. Ya. Brodskii, I. P. Venediktov, S. V. Golubev andd V. G. Zorin, and I. A. Kossyi. Nonequilibrium microwave discharge in air at atmospheric pressure. *Sov. Tech. Phys. Lett.*, 10(2):77–79, February 1984.

[9] Yu.Ya. Brodskii, S.V. Golubev, V.G. Zorin, A.G. Luchinin, and V.E. Semenov. New mechanism of gasdynamic propagation of a discharge. *Soviet Physics JETP*, 57(5):989–993, May 1983.

[10] V.M. Batenin, I.I. Klimovskii, G.V. Lysov, and V.N. Troitskii, editors. *Superhigh Frequency Generators of Plasma*, pages 97–109. CRC Press, Inc, 1994.

[11] A.V. Gaponov-Grekhov and V.L. Granatstein, editors. *Applications of High-Power Microwaves*, pages 147–156. Artech House, INC, 1994.

[12] A.L. Vikharev, V.B. Gil'denburg, S.V. Golubev, B.G. Eremin, O.A. Ivanov, A.G. Litvak, A.N. Stepanov, and A.D. Yunakovskii. Nonlinear dynamics of a freely localized microwave discharge in an electromagnetic wave beam. *Soviet Physics JETP*, 67(4):724–728, April 1988.

[13] A.L. Vikharev, A.M. Gorbachev, O.A. Ivanov, and A.L. Kolysko. Plasma parameters and stimulated uv emission of filamentary structures in a high-pressure microwave discharge. *JETP*, 79(1):94–101, July 1994.

[14] Y. Hidaka, E.M. Choi, I. Mastovsky, M.A. Shapiro, J.R. Sirigiri, and R.J. Temkin. Filamentary arrays in breakdown plasmas generated by a 1.5 mw, 110ghz gyrotron. In *Proceeding of The Joint 32nd International Conference on Infrared and Millimeter Waves and 15th International Conference on Terahertz Electronics*, pages 516–517, 2007.

[15] Kantrowitz. Propulsion to orbit by ground-based lasers. *Astronautics and Aeronautics*, 10(5):74–76, May 1972.

[16] L.N. Myrabo, D.G. Messitt, and F.B. Mead Jr. Ground and flight tests of a laser propelled vehicle. AIAA Paper No. 98-1001, American Institute of Aeronautics and Astronautics, 1998.

[17] L.N. Myrabo. World record flights of beamed-riding rocket lightcraft: Demonstration of disruptive propulsion technology. AIAA Paper No. 2001-3798, American Institute of Aeronautics and Astronautics, 2001.

[18] J.T.Kare. Laser powered heat exchange rocket for ground-to-orbit launch. *Journal of Propulsion and Power*, 11(3):535–543, 1995.

[19] J.P. Knecht and M.M. Micci. Analysis of a microwave-heated planar propagationg hydrogen plasma. *AIAA Journal*, 26(2):188–194, 1988.

[20] P. Balaam and M.M. Micci. Investigation of free-floation resonant cavity microwave plasmas for propulsion. *Jounal of Propulsion and Power*, 8(1):103–109, 1992.

[21] G. M. Batanov, S. I. Gritsinin, I. A. Kossyy, A. N. Magunov, V. P. Silakov, and N. M. Tarasova. High-pressure microwave discharge. In L.M.Kovrizhnykh, editor, *Plasma Physics and Plasma Electronics*, pages 241–282. Nova Science Publishers Commack, 1989.

[22] K.L.G. Parkin and F.E.C. Culick. Feasibility and performance of the microwave thermal rocket launcher. In Kimiya Komurasaki, editor, *Beamed Energy Propulsion: Second International Symposium on Beamed Energy Propulsion*, pages 407–417. American Institute of Physics, 2003.

[23] K.L.G. Parkin, L.D.DiDomenico, and F.E.C. Culick. The microwave thermal thruster concept. In Kimiya Komurasaki, editor, *Beamed Energy Propulsion: Second International Symposium on Beamed Energy Propulsion*, pages 418–429. American Institute of Physics, 2003.

[24] A.R. Bruccoleri, K.L.G. Parkin, and M. Barmartz. Axial temperature behavior of a heat exchanger tube for microwave thermal rockets. *Journal of Propulsion and Power*, 23(4):889–894, 2007.

[25] H. Katsurayama, K. Komurasaki, A. Momozawa, and Y. Arakawa. Numerical and engine cycle analyses of a pulse laser ramjet vehicle. *Transactions of JSASS, Space Technology Japan*, 1:9–16, 2003.

[26] H. Katsurayama, M. Ushio, K. Komurasaki, and Y. Arakawa. Analytical study on flight performance of an air-breathing RP laser launcher. AIAA Paper No. 2004-3585, 40th AIAA/ASME/SAE/ASEE Joint Propulsion Conference and Exhibit, 2004.

[27] H. Katsurayama, K. Komurasaki, and Y. Arakawa. Feasibility for the orbital launch by pulse laser propulsion. *Journal of Space Technology and Science*, 20(2):32–42, 2005.

[28] T. Nakagawa, Y. Mihara, K. Komurasaki, K. Takahashi, K. Sakamoto, and T. Imai. Propulsive impulse measurement of a microwave-boosted vehicle in the atmosphere. *Journal of Spacecraft and Rockets*, 41(1):151–153, 2003.

[29] T. Bussing and G. Pappas. An introduction to pulse detonation engines. AIAA Paper No. 94-0263, 32nd Aerospace Science Meeting and Exhibition, 1994.

[30] T. Endo, Kasahara J., Matsuo A., Inaba K., Sato S., and T. Fujiwara. Pressure history at the thrust wall of simplified pulse detonation engine. *AIAA Journal*, 42(9):1921–1930, 2004.

[31] L.D. Landau and E.M. Lifshitz. *Fluid Mechanics*, volume 6 of *Landau and Lifshitz:Course of Theoretical Physics*, pages 489–494. Butterworth-Heinemann, 2nd english edition, 1984.

[32] A. Sashoh, M. Kister, N. Urabe, and K. Takayama. Laser-powered launch in tube. *Transaction of Japan Society of Aeronatics and Space Science*, 46(151):52–54, 2003.

[33] W.O.Schall, L.Bohn W, H.A.Echkel, W.Mayerhofer, W.Riede, and E.Zeyfang. Lightcraft experiment in germany. In C.R.Phipps, editor, *Proceedings of the SPIE: High-Power Laser Ablation III*, pages 472–481. International Society for Optical Engineering, 2000.

Acknowledgments

I would like to express my gratitude to Associate Professor Kimiya Komurasaki. For six years, owing to his excellent advice and encouragements, I could resolve many experimental and theoretical problems.

I'm grateful to Professor Yoshihiro Arakawa (Department of Aeronautics and Astronautics) for his advice and discussion.

I'm also grateful to Dr. Keishi Sakamoto (Plasma Heating Laboratory, Naka fusion research center, Japan Atomic Energy Agency) for giving me an opportunity of experiments at JAEA. Gratitude is also extended to Mr. Atsushi Kasugai and Dr. Koji Takahashi for cooperating experiments, Professor Tsuyoshi Imai (Tsukuba University) for his advice. Gratitude is also extended to Dr. Ken Kajiwara, Dr. Ryutaro Minami, Mr. Shinji Komori, and Mr. Yukiharu Ikeda on the operation of the gyrotron for the experiment.

I thanks to elders and betters at the University of Tokyo: Dr. Hiroshi Katsurayama (ISAS/JAXA), Dr. Koichi Mori (Nagoya University), Dr. Naoji Yamamoto (Kyushu University) and Dr. Makoto Matsui (The university of Tokyo) for their fruitful discussion.

I'm obliged to Mr. Teppei Shibata and Mr. Yuya Shiraishi, members in Microwave Propulsion group. Mr. Koichi Kawamura and Mr. Masato Ushio helped the experiments before 2005.

Finally, I wish to thank all members in Arakawa-Komurasaki laboratory who propose a comfortable atmosphere.